

University of Dundee

A Finite Element approach for determining the full load-displacement relationship of axially-loaded shallow screw anchors, incorporating installation effects

Cerfontaine, Benjamin; Knappett, Jonathan; Brown, Michael; Davidson, Craig; Al-Baghdadi, Therar; Sharif, Yaseen

Published in:
Canadian Geotechnical Journal

DOI:
[10.1139/cgj-2019-0548](https://doi.org/10.1139/cgj-2019-0548)

Publication date:
2021

Document Version
Peer reviewed version

[Link to publication in Discovery Research Portal](#)

Citation for published version (APA):

Cerfontaine, B., Knappett, J., Brown, M., Davidson, C., Al-Baghdadi, T., Sharif, Y., Brennan, A., Augarde, C., Coombs, W. M., Wang, L., Blake, A., Richards, D. J., & Ball, J. D. (2021). A Finite Element approach for determining the full load-displacement relationship of axially-loaded shallow screw anchors, incorporating installation effects. *Canadian Geotechnical Journal*, 58(4), 565-582. <https://doi.org/10.1139/cgj-2019-0548>

General rights

Copyright and moral rights for the publications made accessible in Discovery Research Portal are retained by the authors and/or other copyright owners and it is a condition of accessing publications that users recognise and abide by the legal requirements associated with these rights.

- Users may download and print one copy of any publication from Discovery Research Portal for the purpose of private study or research.
- You may not further distribute the material or use it for any profit-making activity or commercial gain.
- You may freely distribute the URL identifying the publication in the public portal.

Take down policy

If you believe that this document breaches copyright please contact us providing details, and we will remove access to the work immediately and investigate your claim.

Title

A Finite Element approach for determining the full load-displacement relationship of axially-loaded shallow screw anchors, incorporating installation effects

Author list

Benjamin Cerfontaine*, Jonathan A. Knappett, Michael J. Brown, Craig S. Davidson, Therar Al-Baghdadi, Yaseen U. Sharif, Andrew Brennan, Charles Augarde, William M. Coombs, Lei Wang, Anthony Blake, David J. Richards and Jon Ball

**Corresponding author*

Author details

Benjamin Cerfontaine, BSc, MSc, PhD

MSCA Research Fellow, School of Science and Engineering, University of Dundee, Fulton Building, Dundee, DD1 4HN, UK

ORCID: 0000-0002-4833-9412

Email: b.cerfontaine@dundee.ac.uk

Jonathan A. Knappett, MA MEng PhD GMICE

Professor, School of Science and Engineering, University of Dundee, Fulton Building, Dundee, DD1 4HN, UK

ORCID: 0000-0003-1936-881X

Email: j.a.knappett@dundee.ac.uk

Michael J. Brown, BEng PhD GMICE

Reader, School of Science and Engineering, University of Dundee, Fulton Building, Dundee, DD1 4HN, UK

ORCID: 0000-0001-6770-4836

Email: m.j.z.brown@dundee.ac.uk

Craig Davidson, BSc MSc

Research Associate, School of Science and Engineering, University of Dundee, Fulton Building, Dundee, DD1 4HN, UK

ORCID: 0000-0002-4843-5498

Email: c.s.davidson@dundee.ac.uk

Therar Al-Baghdadi, BSc, MSc, PhD

Geotechnical Engineer, Municipality of Karbala, Karbala, Iraq

ORCID: 0000-0002-7368-4285

Email: therarb@yahoo.co.uk

Yaseen U Sharif, BSc, MSc

PhD student, School of Science and Engineering, University of Dundee, Fulton Building, Dundee, DD1 4HN, UK

ORCID: 0000-0002-3620-7500

Email: y.u.sharif@dundee.ac.uk

Andrew J. Brennan, MEng PhD GMICE

Senior Lecturer, School of Science and Engineering, University of Dundee, Fulton Building, Dundee, DD1 4HN, UK

ORCID: 0000-0002-8322-0126

Email: a.j.brennan@dundee.ac.uk

Charles Augarde, BSc MSc DPhil CEng FICE

Professor, Department of Engineering, Durham University, Durham, DH1 3LE, UK

ORCID: 0000-0002-5576-7853

Email: charles.augarde@durham.ac.uk

Will M. Coombs, MEng PhD

Associate Professor, Department of Engineering, Durham University, Durham, DH1 3LE, UK

ORCID: 0000-0003-2099-1676

Email: w.m.coombs@durham.ac.uk

Lei Wang, PhD

Research Assistant, Department of Engineering, Durham University, Durham, DH1 3LE, UK

Email: lei.wang@durham.ac.uk

Anthony Blake, BEng, PhD

Research Fellow, Faculty of Engineering and the Environment, University of Southampton, SO17 1BJ, UK

ORCID: 0000-0001-5718-7900

Email: a.p.blake@soton.ac.uk

David J. Richards, BEng MSc PhD CEng MICE

Professor, Faculty of Engineering and the Environment, University of Southampton,
UK

ORCID: 0000-0002-3819-7297

Email: [djrsoton.ac.uk](mailto:djr@soton.ac.uk)

Jon Ball, EurGeol Bsc. (Hons) CGeol FGS

Chief Geotechnical Engineer, Roger Bullivant Ltd, Swadlincote, UK

Email: Jon.Ball@roger-bullivant.co.uk

Main text word count: 7602

Number of tables: 6

1 Number of Figures: 16

2 **A Finite Element approach for determining the full load-**
3 **displacement relationship of axially-loaded shallow screw anchors,**
4 **incorporating installation effects**

5
6 B. Cerfontaine*, Jonathan A. Knappett, Michael J. Brown, Craig S. Davidson, Therar Al-
7 Baghdadi, Andrew J. Brennan, Charles Augarde, William M. Coombs, Lei Wang, Anthony
8 Blake, David J. Richards and Jon Ball

9
10 **ABSTRACT**

11 Screw anchors have been recognised as an innovative solution to support offshore jacket
12 structures and floating systems, due to their low noise installation and potential enhanced
13 uplift capacity. Results published in the literature have shown that for both fixed and floating
14 applications, the tension capacity is critical for design but may be poorly predicted by
15 current empirical design approaches. These methods also do not capture the load-
16 displacement behaviour, which is critical for quantifying performance under working loads.
17 In this paper, a Finite Element methodology has been developed to predict the full tensile
18 load-displacement response of shallow screw anchors installed in sand for practical use,
19 incorporating the effects of a pitch-matched installation. The methodology is based on a
20 two-step process. An initial simulation, based on wished-in-place conditions, enables the
21 identification of the failure mechanism as well as the shear strain distribution at failure. A
22 second simulation refines the anchor capacity using soil-soil interface finite elements along
23 the failure surface previously identified and also models installation through successive
24 loading/unloading of the screw anchor at different embedment depths. The methodology is

25 validated against previously published centrifuge test results. A simplified numerical
26 approach has been derived to approximate the results in a single step.

27

28 **KEYWORDS**

29 Screw anchor, Helical Pile, Sand, Finite element modelling, Design

30

31 **INTRODUCTION**

32 Screw anchors or piles are a foundation technology that may provide significant uplift
33 capacity for offshore applications (Byrne and Houlsby 2015; Houlsby 2016) while avoiding
34 pile driving nuisance for marine inhabitants (Bailey et al. 2010). Screw anchors consist of one
35 or more steel helices (150-400mm diameter), attached to a core of smaller diameter and are
36 used onshore to anchor relatively light structures (Perko 2009). These anchors are screwed
37 into the soil by applying a torque and a crowd force to ensure penetration with a minimum
38 soil disturbance (Perko 2009). Such anchors, if appropriately scaled-up, may be suitable to
39 provide the very large tension requirements of bottom-fixed jacket structures (e.g. 20MN,
40 (Byrne and Houlsby 2015)) or floating tension-leg platforms (e.g. 10MN, (Bachynski and
41 Moan 2014)) for offshore wind turbines.

42

43 The uplift capacity of shallow screw anchors was investigated by Davidson et al. (2019)
44 through centrifuge testing in medium-dense and dense sand. The centrifuge uplift capacities
45 were compared with results published in the literature, as shown in Figure 1. This figure
46 presents a non-dimensional bearing factor, N_y , obtained by normalising the uplift capacity
47 with respect to the helix embedment depth H , the area of the helix and the buoyant unit
48 weight γ' ,

$$N_y = \frac{F_y}{\gamma HA}. \quad (0)$$

49 Centrifuge results are consistent with the other experimental results, as shown in Figure 1.
50 Bearing factors obtained by Ilamparuthi et al. (2002) constitute the upper bound of the
51 results presented, especially at larger relative embedment. This is probably due to their
52 relatively small scale, being tested at 1g, leading to a more pronounced effect of dilatancy on
53 the soil response. Conversely, centrifuge tests provide a lower bound. Centrifuge results of
54 Dickin (1988) were reported for comparison, but were related to square plate anchors,
55 which have been shown to provide lower uplift capacity (Giampa et al. 2018a).

56

57 Byrne and Houlsby (2015) stated that multi-footing structures such as tripods or jacket
58 structures will become necessary to deploy wind turbines in deeper water. In this case, the
59 tensile capacity is the critical design case and screw anchors can provide sufficient capacity.
60 However typical analytical approaches (e.g. Mitsch and Clemence 1985) may significantly
61 overpredict the screw anchor capacity for these large scale applications. The recent semi-
62 analytical method proposed by Giampa *et al.* (2017) for shallow anchors which is based on
63 peak friction and dilatancy angles for shallow anchors, assumes that the failure mechanism
64 can be described by a shallow wedge, whose inclination to the vertical direction is equal to
65 the dilatancy angle. This finding is similar to the work of White et al. (2008) for the uplift of
66 buried pipelines and has been theoretically justified for anchors by Vermeer and Sutjiadi
67 (1985). However, the method is limited to single helix screw anchors and does not provide
68 any load-displacement (stiffness) information, which is very important for jacket structures
69 and tension-leg platforms, as the axial stiffness controls the global rotational stiffness of the
70 wind turbines. For instance, the rotation of bottom-fixed wind turbines must typically be
71 kept below 0.5° to ensure safe operation (Achmus *et al.* 2009).

72

73 Finite Element modelling enables the prediction of the entire tensile load-displacement
74 relationship, but few studies have previously tackled this problem for screw anchors in
75 cohesionless soils due to the difficulties in capturing the effects of installation (a large
76 displacement process) on capacity. Those approaches which have been proposed for
77 modelling the problem rely on back-calculated parameters, characterising the soil properties
78 around the anchor, to reproduce field or experimental tests (e.g. Papadopoulou et al. 2014;
79 Mosquera et al. 2015; Perez et al. 2018) without which uplift capacities are overestimated
80 (e.g. Gavin et al. 2014) due to an incorrect modelling of the strength mobilised at failure. On
81 the other hand, the installation process is a large deformation process which strongly
82 modifies the void ratio (e.g. tomography results presented in Schiavon (2016)) and stress
83 state around the anchor, modifying the stiffness of the anchor. Giampa et al. (2017) used
84 limit analysis and finite element methods to simulate small-scale 1g tests. However, they
85 focused on anchor capacity and did not provide any comparison of the load-displacement
86 behaviour or initial stiffness. Consequently, there is a need to develop a new methodology to
87 better predict both the uplift capacity and initial stiffness that does not rely physical testing
88 for deriving global empirical parameters and which is simple enough to be used in the
89 practical design of screw anchors.

90

91 The objective of this study is to define a flexible methodology to predict drained tensile
92 performance of shallow screw anchors representative of offshore applications (full load-
93 displacement behaviour, incorporating capacity and stiffness) using the Finite Element
94 method in 2D axisymmetric conditions, which accounts for the effects of a drained
95 installation process in a simplified way. This method is based on a well-defined numerical

96 procedure requiring measurable, rather than arbitrarily defined soil parameters and is
97 applicable to a range of geometries (helix number and spacing). This will address the key
98 limitations of existing analytical and numerical capacity models and will provide a method
99 for determining both stiffness (as necessary to calculate natural frequencies of a foundation-
100 renewable device system) and capacity (i.e. a virtual load test) for informing practical design.
101 Single and double large helix diameter screw anchor centrifuge load tests, published by
102 (Davidson et al. 2020) and wished-in-place typical onshore screw anchors Hao et al. (2018),
103 will be used to validate the finite element analyses. The shape of the failure mechanism, the
104 stress and strain distributions along the failure mechanism are key variables that are studied
105 in detail in order to develop a reliable method for design.

106

107 **PHYSICAL AND NUMERICAL MODELS**

108 The Finite Element (FE) method cannot be used to reproduce the exact large-deformation
109 installation process, with other methods being preferable (Wang et al. 2017). However, the
110 FE method offers a good compromise between the simulation cost and accuracy of results.
111 The objective of this work is to develop a modelling approach that is practically applicable in
112 the design screw anchors for offshore applications. Consequently, it must be achievable
113 within commercial software (e.g. PLAXIS software (PLAXIS 2017a)), it must be fast (2D
114 axisymmetric analysis) and it must be based on typical constitutive models (e.g. the
115 Hardening soil model (Schanz et al. 1999a)) relying on a limited number of measurable
116 parameters that can be determined using routine laboratory and in-situ test methods. The
117 numerical modelling methodology as well as physical (centrifuge) models used to validate it
118 are described in this section.

119

120 **Centrifuge tests**

121 Numerical results are validated against two sets of small-scale centrifuge tests undertaken at
122 the University of Dundee (UoD) (Davidson et al. 2019) and the University of Western
123 Australia (UWA) (Hao et al. 2018), both in dense sand. Prototype geometries and important
124 variables are summarised in Table 1, along with tensile capacity F_y .

125

126 The tests undertaken at the University of Dundee, extensively described in (Davidson et al.
127 2019) incorporate the installation effect. Three screw anchors were installed in a very dense
128 sand (referred to as VD, $D_r = 84\%$ on average) and one in a medium dense sand (MD, $D_r =$
129 57%). The tests were undertaken in dry sand at 48g. The stress field generated within the
130 sand box was identical to the effective stress field that would be obtained in a saturated
131 sand at 80g – an approach explained and justified in Li et al. (2010). This approach has
132 previously been validated for lateral pile loading by Klinkvort et al. (2013). The helix
133 diameter D_h of all model anchors installed in very dense sand was equal to 1.7m at prototype
134 scale (scaling factor equal to 80g). Two of these models (U1VD-A and U1VD-B) had a single
135 helix while the third one (U2VD) possessed two helices whose spacing was equal to 2 helix
136 diameters. The helix diameter of the model (U1MD) installed in medium-dense sand was
137 equal to 3.4m. The core diameter D_c was equal to 0.88m for very dense sand models and
138 1.13m for the medium-dense sand. The helix pitch was constant and equal to 0.56m. All
139 models were installed at a constant rotation rate equal to 3RPM. The advancement rate was
140 chosen to equal one helix pitch per revolution to limit disturbance, i.e. pitch-matched
141 installation as recommended in the literature (Perko 2000). The vertical load or crowd force
142 ($F_{y,min}$) required to maintain the prescribed penetration rate of the model was recorded
143 during the test. The installation process and the uplift loading in both centrifuge tests and

144 numerical simulations were imposed sufficiently slow to represent drained installation and
145 loading conditions, representative of the offshore conditions. The tests were also modelled
146 dry to assure this was the case as mentioned previously.

147

148 The second set of data used for independent validation consists of tests published by Hao et
149 al. (2018). These tests consist of flat plate and helical plate anchors (0.4m diameter) were
150 placed into a strongbox and the sand was pluviated all around them, before each anchor was
151 tested in tension. In this case, there is no installation effect and the model anchors can be
152 considered as experimentally wished-in-place. The target global density of the different
153 samples ranged between 85% and 96% and the samples were spun at 20g. The helix
154 diameter D_h at the prototype scale was equal to 0.4m while the core diameter D_c was equal
155 to 0.094m. The helix pitch was constant and equal to 0.1m at prototype scale.

156

157 General scaling laws and practical recommendations were respected to ensure the similitude
158 of centrifuge tests at prototype scale (Garnier et al. 2007). The diameter of the smallest
159 helix/plate (D_h) to the mean grain size (d_{50}) considered here exceeds 150. If it is assumed that
160 helix behaviour is controlled by shear band propagation, this value must exceed the range of
161 50 to 100 recommended in Garnier et al. (2007). Additionally, this also exceeds the
162 recommendations in for grain size effects on pull out of anchors reported by Garnier et al.
163 (2007) of plate width, B ratio to d_{50} of greater than 48. In addition, the helix pitch to d_{50} ratio
164 was larger than 50, which was assumed adequate to allow the movement of all particles
165 throughout the helix during the installation process. Studies based upon Discrete Element
166 modelling (DEM) with far fewer particles actually modelled between the helix plates showed
167 good correlations with centrifuge testing (Sharif et al. 2019). The smallest pile shaft diameter

168 gave a minimum value of $79d_{50}$ satisfying the lower bound recommendation in Garnier et al.
169 (2007) of 50 times d_{50} regarding the ratio of pile to average grain size diameter.

170

171 ***Geometry of the numerical model***

172 In terms of screw pile geometry it is common to idealise the helices as horizontal plates connected to
173 the pile core at a depth representative of the mid pitch of the true helix (Livneh and El Naggar 2008;
174 Al-Baghdadi 2018; Pérez et al. 2018). This hypothesis has been tested through centrifuge
175 experiments on wished-in-place (WIP) screw anchors by Hao et al. (2018), who showed that the uplift
176 capacity of flat and helical plates was almost identical. A similar result was found numerically for WIP
177 anchors by (Al-Baghdadi 2018). This simplification allows screw anchors to be modelled under
178 axisymmetric conditions due to the symmetry of the geometry and loading (in tension or
179 compression). The anchor elements were here modelled using 5-node plate elements based on
180 Reissner-Mindlin's theory (Zienkiewicz and Taylor 2000). The properties of the plates, matching the
181 centrifuge models, are reported in Table 2. The anchor and helix structural behaviour was assumed
182 to be purely elastic. Elastic structural response was observed for all centrifuge test cases considered
183 and would be desirable in design. The thickness of the plate and helix used at UWA was not specified,
184 therefore they were assumed very stiff and the same helix/plate properties were used for all tests.

185

186 The soil was modelled by 15-node triangular 2D axisymmetric elements. The mesh was
187 chosen to be a good compromise between accuracy of results and CPU time required for
188 simulations. It was different for each geometry, but all meshes were refined close to the
189 helices and in a zone extending to $3.5D_h$ from the anchor core so that failure surface could
190 be modelled with enough precision. The boundary conditions were representative of the
191 centrifuge tests in each case and were sufficiently spaced from the screw anchors to avoid
192 any interference. The bottom boundary lies $7D_h/10D_h$ below the helix while the lateral

193 boundary was located $17D_h/30D_h$ from the core for UoD and UWA tests respectively. The
194 displacement was fully fixed along the bottom boundary and normally fixed (i.e. allowing
195 vertical displacement) along the vertical boundaries. The numbers of elements used for each
196 screw anchor mesh are reported in Table 3. A force (for load-controlled stages during
197 installation modelling) or displacement (for displacement-controlled virtual load test) was
198 applied at the top of the shaft to be consistent with the centrifuge experiments.

199

200 Zero-thickness 5-node interface elements were used to simulate the interactions between
201 the helix/core and the soil or shear bands within the soil (see later). They were defined on
202 each side of the plate elements. These interface elements allow the opening of a gap
203 between plate and soil when the contact stresses reduce to zero, as well as tangential sliding
204 after friction mobilisation.

205

206 ***Soil constitutive model***

207 The ‘hardening soil model with small strain stiffness’ (HSsmall) was adopted to simulate the
208 sand behaviour (Schanz 1998; Schanz et al. 1999b; PLAXIS 2017b). The parameters of the
209 HST95 Congleton sand, used for the centrifuge tests at the UoD, have been calibrated
210 previously against laboratory element tests as described elsewhere (Lauder et al. 2013; Al-
211 Defae et al. 2013). The use of this model has been comprehensively validated against 1-g,
212 centrifuge and field tests, encompassing various boundary value problems, including piles
213 (e.g. Al-Defae *et al.* 2013; Knappett *et al.* 2016; Al-Baghdadi *et al.* 2017).

214

215 The constitutive model is composed of a shear-strain hardening yield surface. It assumes
216 that the stress and strain describe a hyperbolic relationship for the primary triaxial loading of

217 a soil sample and the yield surface converges towards the Mohr-Coulomb surface. It
218 encompasses a tension cut-off to prevent tension loading of the soil and a second volumetric
219 strain hardening yield surface to reproduce oedometric stress paths. The model stiffness is
220 confinement dependent and secant stiffness degrades as shear strain increases. The
221 unloading/reloading elastic stiffness is not a function of the shear strain. The volumetric
222 behaviour is non-associated and is related to the dilatancy angle as reported elsewhere
223 (PLAXIS 2017b). It includes a dilatancy cut-off, ensuring the current void ratio remains lower
224 or equal to the maximum void ratio. All parameters used for the very-dense and medium-
225 dense models are reported in Table 4. They were previously determined for a large range of
226 relative densities based on shearbox and oedometer tests by Al-Defae *et al.* (2013) and were
227 subsequently further validated against drained triaxial compression tests.

228

229 The UWA samples were prepared in a dry fine to medium sub-angular silica sand, at relative
230 densities ranging from 85% to 96%. There is no published triaxial data to calibrate the
231 HSsmall model parameters, only the critical state friction angle ϕ'_{cv} ($\approx 31^\circ$) was provided in
232 the paper and the authors assumed that the peak friction angle ϕ'_{pk} could be calculated
233 according to

$$\phi'_{pk} = \phi'_{cv} + m_{tr} I_R \quad (0)$$

234 where I_R is the relative dilatancy angle and $m_{tr}=3$ for triaxial conditions are obtained from
235 (Bolton 1986).

$$I_R = 5D_r - 1. \quad (0)$$

236 The resulting peak friction angles range from 41.2° to 42.4° respectively. The dilatancy angle
237 was selected to be consistent with the formulation of the hardening soil model (Schanz and
238 Vermeer 1996)

$$\sin \psi'_{pk} = \frac{\sin \phi'_{pk} - \sin \phi'_{cv}}{1 - \sin \phi'_{pk} \sin \phi'_{cv}} \quad (0)$$

239 for which the dilatancy index ranges from 12.3° to 14.1°. The buoyant unit weight varies
 240 between 10.5 and 10.6kN/m³. The rest of the parameters, especially stiffness parameters,
 241 are assumed to be identical to the HST95 sand parameters and are defined as a function of
 242 the relative density in Table 4.

243 The interface behaviour was also described by the HSsmall model. For the soil-steel interface
 244 elements, the friction and dilatancy angle were defined equal to 27° and 0° respectively,
 245 (Lauder et al. 2013). The dilatancy angle of the soil-soil interface at the critical state was set
 246 equal to zero while it remained equal to the peak value otherwise. The soil was assumed
 247 completely saturated (with a fully drained response) and the water level was located at the
 248 soil surface.

249

250 ***Modelling methodology***

251 The methodology developed to capture both a consistent anchor capacity and stiffness is
 252 described here and summarised in Figure 2. The methodology is based on two successive
 253 numerical simulations of increasing complexity (stages 1 and 2), with output from the first
 254 stage informing the second. This multi-stage approach allows for the effects of installation-
 255 induced soil stress distribution disturbance to be modelled in a self-contained and
 256 approximate way, without requiring centrifuge or field load test data to back-calculate
 257 appropriate soil parameters in disturbed soil, and is therefore a significant improvement for
 258 practical application compared to the recent method of Perez et al. (2018). It is based only
 259 on known geometrical parameters of the screw anchor, the in-situ relative density, which in
 260 sands can be used to determine the required soil parameters (Table 4), and the measured
 261 crowd force during installation. This final parameter can be predicted using the CPT-based

262 relationships presented by Davidson et al. (2018), and can subsequently be refined using
263 measurements from the installation rig in the field or on the centrifuge. However, this
264 procedure does not reproduce the soil displacement due to the shaft penetration and helix
265 movement. The extrapolation of the results to geometries inducing significantly larger or
266 lower shaft diameters should then be done cautiously.

267

268 The stage 1 simulations (Figure 2(a)) were based on the minimal number of hypotheses and
269 composed of three distinct phases. Firstly, the geostatic stress field distribution was
270 initialised within the soil. The initial distribution of the horizontal stresses was based on the
271 Jaky formula (Jaky 1944) and the screw anchor is considered to be wished-in-place at a
272 depth corresponding to each test. Secondly, the compression load corresponding to the
273 recorded installation crowd force at the final helix depth was applied under load control,
274 then reduced to zero (simulating removal of the installation rig). Finally, a vertical upward
275 displacement was imposed at the top of the core to simulate the uplift. The numerical
276 simulations were stopped when the ultimate capacity was reached which corresponds to
277 vertical displacements ranging from 0.1 to 0.3D_n. Failure of the anchor corresponds to a peak
278 or plateau in the load-displacement relationship and the formation of an uplift failure
279 mechanism, as reported in Figure 2(a).

280

281 In stage 2, the numerical model was enhanced to improve the prediction of both anchor
282 capacity and initial stiffness. To improve the capacity prediction (Figure 2(b)), discrete soil-
283 soil interface elements, oriented along the shear plane locations identified from stage 1,
284 were introduced in the mesh, as shown in Figure 2(b). Reduced strength parameters,
285 corresponding to localised soil softening, were defined over a limited zone, based on the

286 analysis of the magnitudes of the shear strains, as shown in Figure 2(b). This analysis is made
287 by inspection of shear strain contour plots at failure (peak or plateau in the load-
288 displacement relationship) from stage 1 simulations. It can be assumed that the soil will
289 enter the post-peak softening regime for shear strain larger than a given threshold. This
290 variable can be obtained from experiments, e.g. as the strain at which critical state strength
291 is achieved from a direct shear test. For the HST95 sand, it is approximately 7.5% as in (Al-
292 Defae et al. 2013), or approximately 15% from triaxial tests (Robinson 2016). For the cases
293 presented herein, this threshold strain was assumed equal to be 10% for the HST95 sand
294 used by Davidson et al. (2019) and it was assumed identical for application to the results of
295 (Hao et al. 2018) as no specific element test results for this case were available. The distance
296 over which a shear strength corresponding to the critical state parameter can then be
297 identified by inspection of the shear strain contour in the FE software. The corresponding
298 interface properties are then assigned to two different zones, corresponding to the softening
299 and peak states.

300 This approach can be defined as a hybrid FE-Limit Analysis and has several advantages for
301 practical design. It incorporates the effect of soil volumetric compression on the failure
302 mechanism, unlike Limit Analysis (as reported in Cerfontaine et al. 2019). In addition, the
303 approach does not require complex numerical solutions to avoid problems resulting from
304 the use of strain-softening models (Anastasopoulos et al. 2007). Indeed, real shear bands
305 have the width of several sand grains (5 to $40d_{50}$, where d_{50} is mean particle size of the sand
306 (Desrues and Viggiani 2004; Lauder et al. 2012)), which reduces almost to a zero-thickness
307 interface at the scale of a boundary value problem. The rigorous simulation of such shear
308 bands would require an extremely fine mesh (size equal to approximately $3d_{50}$; Gudehus

309 and Nübel 2004) or regularisation techniques introducing some mesh-size dependence, (e.g.
310 Anastasopoulos et al. 2007).

311 Also, in stage 2 (Figure 2(c)), the stiffness prediction was improved by considering the stress
312 field modification around the anchor due to the varying crowd force applied during its
313 installation. Indeed, this force induces settlement and generates soil hardening over a zone
314 which is several helix diameters wide around the anchor. This installation effect is
315 approximated by simulating several loading/unloading phases, as depicted in Figure 2(c),
316 where the compression force applied corresponds to the position of the helix at a given
317 depth. This loading/unloading is applied at five successive depths to simulate the installation
318 process. Only the structural elements of the screw anchors above this depth are activated,
319 which is similar to the press-replace method developed for displacement piles (Engin et al.
320 2015), where soil elements are progressively replaced by pile elements to simulate its
321 installation. The compressive stress bulb beneath a helix plate extended to approximately
322 $4D_h$ below it. Therefore, it was decided to apply a compression step every $1.5D_h$, to ensure
323 the soil would be relatively uniformly preloaded, while maintaining the complexity of the
324 mesh and computational time to a reasonable level. This distance is lower than the limit for
325 helix interaction in compression, equal to $2D_h$ (Al-Baghdadi 2018). A simulation based on 7
326 installation steps did not show any difference in the load-displacement relationship. The
327 crowd forces applied in these phases can be either predicted by the CPT method proposed in
328 (Davidson et al. 2018) or values from the installation rig.

329 ***Mesh influence***

330 Five different meshes with increasing number of elements were considered, to assess the
331 influence of the mesh size on the results of the stage 1 simulations. The overall number of
332 elements was set up by the user and the size of elements automatically adapted by the

333 software. The initial stiffness and hardening phases were very similar for the different
334 number of elements. Therefore, only the capacity at $0.1D_h$ and at peak were compared.
335 Results are reported in Table 5 and show that the peak capacity increases with the number
336 of elements and mesh refinement, although this increase is very small between meshes #4
337 and #5. The simulation related to the mesh 1 stopped converging before the end of the
338 simulation. The inspection of the shear strain field show that the shear band is narrower and
339 more marked as the mesh refinement increases, as would be expected. The overall
340 variability of the anchor capacity is limited, especially with respect to the variability that
341 could be expected for real case studies. The choice of a mesh was then based on the CPU
342 time required to obtain simulation results. The mesh #4 (3175 elements) was adopted as a
343 good balance between mesh refinement and calculation time.

344

345 **VALIDATION AGAINST CENTRIFUGE TESTS**

346 This section compares the numerical simulations with the centrifuge tests. The key variables
347 (stress and strain fields) are analysed to illustrate how the methodology was developed and
348 explain how it affects the final results.

349 ***Wished-in-place anchors (UWA)***

350 The enhancement of the capacity was validated first against wished-in-place tests of UWA.
351 The two-stage procedure was applied, but only the capacity was enhanced, as there was no
352 installation effect to take into consideration. The extent of the failure mechanism was
353 inspected in results from stage 1 and the softening zone was applied along the interface
354 elements in stage 2. In this case, this zone was around $2.5D_h$ in length. An example of the
355 load-displacement relationship is illustrated in Figure 3 and shows that the stiffness and
356 capacity are relatively consistent with the Stage 2 simulations, while Stage 1 overpredicts the

357 capacity. The peak capacity was identified for 5 different relative embedment ratios and
358 compared in Figure 4 with centrifuge test reported by Hao et al. (2018). Results at shallow
359 embedment ratios (≤ 9) are relatively consistent with the experimental results, particularly
360 given the greater uncertainty in the selection of some specific soil parameters in these cases.
361 The simulations at the largest relative embedment ratio overpredict the capacity, but a deep
362 failure mechanism (e.g. Meyerhof and Adams (1968)) has clearly been reached in the
363 centrifuge testing, which is out of scope of this study.

364

365 ***Anchors installed in-flight (UoD)***

366 Figure 5 compares the measured prototype centrifuge uplift load with the total vertical
367 reaction load at the top of the anchor shaft, F_y , obtained from the numerical simulations:
368 purely wished-in-place (stage 1), enhanced capacity only (stage 2 - capacity) and full
369 methodology (stage 2 - capacity/stiffness). All results are depicted as a function of the
370 normalised vertical displacement u_y/D_h .

371

372 The initial stiffness of wished-in-place simulations (Stage 1) was relatively well captured by
373 the different simulations although the different curves diverged rapidly (at approximately $u_y/D_h=0.01$)
374 for the two single helix anchors embedded in very dense sand, as shown in Figure 5
375 (a, c). However, the maximum loads obtained numerically, corresponding to a fully formed
376 failure mechanism, overpredicted the centrifuge test results in each case, from +25% (U1VD-
377 A) to +43% (U1VD-B). They also overestimated the vertical displacement required to reach
378 this maximum capacity, which was equal to $0.1D_h$ for the centrifuge tests and close to
379 $0.25D_h$ for numerical simulations.

380

381 The enhanced capacity simulations (stage 2 - capacity), incorporating soil-soil interface
382 elements based on stage 1 results, show that the prediction of the uplift capacity was
383 considerably improved for single helix anchors (Figure 5 (a, c)), although the prediction for
384 the double helix case was strongly degraded (Figure 5 (d)). However, the initial stiffness was
385 underpredicted in very dense sand. Detailed discussion of the parameterisation of the soil-
386 soil interface elements resulting in the curves shown in Figure 3 is presented in the following
387 Discussion section.

388

389 Results of the simulations incorporating installation effects (stage 2 - capacity/stiffness)
390 were the most consistent with the centrifuge tests, as depicted in Figure 5. The load-
391 displacement relationship and initial stiffness were more consistent with the centrifuge tests
392 for both single helix anchors embedded in very dense sand compared to previous
393 predictions, as shown in Figure 5 (a, c). The initial stiffness was slightly overpredicted in the
394 medium dense case (Figure 5 (b)). The difference was more pronounced in the double helix
395 case (Figure 5 (d)) and the initial stiffness was almost identical for all three very dense
396 simulations.

397

398 The difference between all those simulations can be explained through the inspection of the
399 failure mechanism (capacity) and stress distribution (stiffness) around the anchor before and
400 at failure. This analysis is undertaken in the following. In addition, the procedure to inspect
401 Stage 1 results to derive Stage 2 simulations is detailed.

402

403 **DISCUSSION**

404 ***Failure mechanisms***

405 Five distinct variables were considered to identify and interpret the uplift failure mechanism
406 for the wished-in-place (Stage 1) simulations. Two of these variables were cumulative over
407 the simulation, namely the vertical displacement u_y and shear strain γ_s , and were therefore
408 influenced by the complete deformation history of the screw anchor. The three other
409 variables were instantaneous for a given load step, namely the increments of vertical
410 displacement Δu_y and shear strain $\Delta \gamma_s$, and the current plastic points (PP, i.e. integration
411 point reaching the plastic yield surface). These variables have been used previously to
412 interpret the failure mechanism of plate anchors embedded in sand (Cerfontaine et al. 2019)
413 and are depicted in Figure 6 for the single deep helix anchor embedded in very dense sand
414 (U1VD-B) as an example. The results show the progressive formation of the failure
415 mechanism, which had not been constrained by soil-soil interface elements at this stage.

416

417 Figure 6(a) describes the state of the soil after applying the (maximum, last recorded) crowd
418 force at the end of installation and unloading to zero compression. It indicates that shear
419 bands pointing towards the developed during the first phase were reactivated (in the
420 opposite direction) during uplift. After $0.1-0.2D_h$ imposed uplift displacement, the failure
421 mechanism was not fully formed as shown in Figure 6(b and c). Several shear bands seemed
422 to initiate from the helix edge at different orientations. The failure mechanism observed in
423 this study was fully formed after a displacement equal to $0.3D_h$ and corresponded to a
424 shallow wedge of soil (i.e. shallow failure mechanism).

425

426 The conical shape of this shallow failure mechanism is consistent with previous experimental
427 studies undertaken for buried anchors (e.g. Ilamparuthi and Muthukrishnaiah 1999; Liu *et al.*
428 2012) where image analysis of the failure mechanism through a Perspex face was

429 undertaken and analytical approaches (e.g. Das and Shukla 2013). However, the exact
430 inclination of this conical mechanism previously reported varied from study-to-study, as
431 described in Cerfontaine et al. (2019) for plate anchors. For the screw anchors considered
432 here, the failure mechanism diverged slightly from a straight line and its orientation was
433 close to the assumed mechanism from Giampa *et al.* (2017), i.e. inclined at the dilatancy
434 angle ($\psi'_{pk} = 17^\circ$ for the very dense sand, indicated by a dashed line in Figure 6) to the vertical
435 direction. This inclination appears consistent with previous theoretical analyses for shallow
436 anchors (Vermeer and Sutjiadi 1985) and experimental evidence for uplifting pipelines
437 (White et al. 2008). Similar conclusions were drawn from interpretation of the medium-
438 dense sand results (not shown). It is noted though that these additional studies do not
439 include installation effects, but still provide some insights into potential failure mechanisms
440 that may be expected in uplift. It is also noted that specific effects of soil density changes
441 due to installation and their subsequent potential effects on the nature of the failure
442 mechanism may not be fully captured in these studies.

443 The failure mechanism of multi-helix anchors depends on the inter-helix spacing. If two
444 adjacent helices of identical diameter are sufficiently close, a cylindrical failure surface,
445 whose diameter is equal to the helix diameter, is assumed to form between them in tension
446 or compression (Tsuha et al. 2007; 2012; Knappett et al. 2014; Al-Baghdadi et al. 2017a). At
447 greater spacing, the helices may act independently. The evolution of the failure mechanism
448 is depicted in Figure 7 at different time steps for the double helix case (U2VD). The failure
449 mechanism occurred for a lower imposed vertical displacement ($0.1D_h$) than the single helix
450 case. It consisted of an inter-helix failure plane and a shallow wedge mechanism, which was
451 oriented along the proposed failure mechanism of Giampa et al. (2017). Figure 7(b-c) show
452 that there was a competition between several shear bands during the uplift of the screw

453 anchor. Additional shear bands were initiated at the edge of the bottom helix or at a position
454 in between the two helices, but they did not reach the surface. In summary, it is clear that
455 for a multi-helix anchor, the embedment depth of the upper helix plate appears to control
456 the apparent wedge-shaped uplift mechanism observed in this study and that at lower
457 displacements there is fluctuation between a cylindrical mechanism and wedging emanating
458 from the lower helix.

459

460 The inspection of results presented in Figure 6 and Figure 7 was used to define the soil-soil
461 interface geometry of stage 2 (enhanced capacity). This allowed the modelling of a greater
462 slip deformation at failure without excessive mesh distortion and to allow strain-dependent
463 softening (at failure) to be incorporated. For single helix anchors, the soil-soil interface
464 elements were inclined at the dilatancy angle to the vertical direction as per (Giampa et al.
465 2017) (shallow wedge). For the double helix case, the interface was set-up similarly from the
466 upper helix, while a cylindrical failure mechanism (vertical interface elements) was enforced
467 between the lower and upper helices.

468

469 Figure 6 shows that large shear strain developed along the failure mechanism in stage 1. It
470 was greater than 30% close to the anchor edge and decreased up to a normalised distance
471 along the failure mechanism ξ/D_h of approximately 2. The distribution then decreased almost
472 linearly up to the surface. Results of experimental triaxial tests (Robinson 2016) as well as
473 direct shear tests reported by Al-Defae et al. (2013) suggest that HST95 sand appears to
474 soften at shear strains greater than 2-3% for medium-dense to dense sand. A larger shear
475 strain is necessary (>10%) before reaching the critical state, depending on the soil density
476 and confinement. Consequently, soil-soil interface properties in the zone closest to the

477 anchor, namely the softening zone, considered that critical state strength was mobilised
478 within the interface after peak. The length of this softened zone was based on the analysis of
479 shear strain contour results from the stage 1 analysis (rather than by back-fitting empirically
480 to match the centrifuge measured capacity). This was approximately $2D_h$ for screw anchors
481 in very dense sand and $2.5D_h$ in medium dense sand. Beyond this zone, the interface
482 properties were identical to the virgin soil properties. It is verified that the pre-definition of a
483 failure-mechanism does not create a new global failure pattern. This is shown in Figure 8 for
484 the single helix case (U1VD-B), where the plastic points, shear strain and vertical
485 displacement all described a wedge failure mechanism whose shape is identical to the pre-
486 defined one.

487

488 ***Stress distribution along the failure mechanism***

489 Most analytical approaches to screw anchor design consider that failure in uplift occurs
490 between rigid soil blocks and assumes a normal shear stress distribution, based on peak
491 friction angle, increasing linearly with depth (Ghaly et al. 1991b; Giampa et al. 2017).
492 However, the soil is far from rigid and significant vertical displacement was required to fully
493 mobilise the failure mechanism, as shown in Figure 5. Subsequently, the load applied by the
494 helix on the soil generated vertical strain. Lateral strain was constrained by the surrounding
495 soil, increasing the lateral stress distribution, as shown numerically by Cerfontaine et al.
496 (2019) for plate anchors or experimentally for screw piles in a pressure chamber (Nagata and
497 Hirata 2005; Nagai et al. 2018). The stress distributions around the anchor and along the slip
498 surface were then modified, such that the normal and shear stresses at failure were
499 increased. Figure 9 (a and b) show the normal and shear stress distributions along the slip
500 surface (inclined at $\theta = 17^\circ$ to the vertical) for the single helix anchor in very dense sand

501 (U1VD-B) for the wished-in-place (Stage 1) simulation. The results are plotted as a function
502 of the normalised distance ξ/D_h from the edge of the helix, in the direction of the slip
503 surface. The results are normalised with respect to the maximum normal and shear stresses
504 assumed in the approach proposed by (Giampa et al. 2018b) since their failure mechanism is
505 identical to the one observed in this study, where:

506

$$\tau_{G,max} = \tan \phi'_{pk} \sigma'_{N,G,max} = \tan \phi'_{pk} \cos(\phi'_{pk} - \psi'_{pk}) \gamma' H \quad (0)$$

507

508 From in Figure 9 (a and b) the maximum values measured were several times those assumed
509 in the (Giampa et al. 2018b) approach (which assumes a rigid block of soil), even after small
510 vertical displacements.

511

512 The stress distribution along the interface is compared for both stages 1 and 2 in Figure 10.
513 Results show that both normal and shear stress distributions are modified (reduced in
514 magnitude) in the softening zone. However, the decrease is more significant for the shear
515 stresses as they are both (i) proportional to the reduced normal effective stresses and (ii) the
516 friction angle is reduced to critical state. Finally, both stress distributions are significantly
517 different from the linear distribution assumed by Giampa et al. (2017, 2018b) (even if the
518 uplift capacity is well approximated) or any other analytical methods. This indicates that the
519 FE method may be preferable to analytical methods, even if only capacity is of interest.

520

521 ***Depth and density effect***

522

523 Additional simulations for relative embedment ranging between $1 \leq H/D_h \leq 8$ for relative
524 densities between 57-84% were conducted to increase the generality of previous
525 observations. Cross-sections along failure planes inclined at the dilatancy angle to the
526 vertical (dilatancy angle is a function of relative density) at each embedment ratio are
527 compared in Figure 11 for $D_r = 84\%$ (as an example). Figure 11(a-b) show that the maximum
528 normal and shear stress at failure increase with depth, which is consistent with observations
529 made by Cerfontaine et al. (2019) for plate anchors.

530

531 The length of the shear band where high shear strain occurs was assessed through a
532 systematic analysis of the shear strain output (cross-sectional strain contour plot such as
533 Figure 6) at failure. A threshold of shear strain above which strain-softening was expected to
534 develop was established, equal to 10% for all simulations and corresponding to the shear
535 strain required to reach the critical state at these densities. The equivalent length of the
536 assumed failure mechanism along which softening occurred is shown in Figure 12. This figure
537 shows that the length of the softening zone was almost equal to zero at $H/D_h=1$ and
538 increased linearly up to a certain depth ($H/D_h = 3$ and 4 for very dense and medium dense
539 sand respectively). Above these normalised depths, the softening zone length appeared to
540 be constant, although some scatter was observed.

541

542 The procedure (addition of soil-soil interface elements) was applied to a single helix screw
543 anchor embedded in both sand densities for a varying embedment ratio. The length of the
544 softening zone was based on results presented in Figure 12. Results in Figure 13 show that
545 the stage 2 simulations generate a significant decrease in bearing capacity. A comparison
546 with the uplift capacity obtained through the approach of Giampa *et al.* (2017) shows that it

547 is consistent with the numerical results, even at larger relative embedment ratios, for a $D_r =$
548 84%, although it should be noted that the postulated stress distribution in that method is
549 different.

550

551 ***Installation effect***

552 The installation procedure mainly affected the stiffness for single plate screw anchors, rather
553 than the capacity, as shown in Figure 5 by comparing the two stage 2 FE curves. In addition,
554 Table 6 shows that the magnitude of the compression load has a limited impact on the
555 ultimate uplift capacity for the single helix screw anchor. An increase or decrease of the
556 crowd force by 50% over the whole installation process, generates only a variation of 7% in
557 the uplift capacity. However, the stiffness is affected by this crowd force magnitude. This can
558 be mechanically explained through the analysis of the unloading/reloading Young modulus
559 E_{UR} and the average stress fields induced around the anchor just before uplifting which are
560 shown in Figure 14.

561

562 The large compression (crowd) force applied during installation had several consequences.
563 Firstly, the soil was sheared over a zone of soil that was several helix diameters in size. As
564 the soil was strained, its secant stiffness decreased (beyond the range of small-strain
565 stiffness). After the soil was loaded in compression up to a deviatoric stress q_{comp} (as shown
566 in Figure 15(a)), the yield surface hardened, and its unloading stiffness was based on the E_{UR}
567 modulus. Consequently, the reloading of the soil during the uplift phase will follow the same
568 path up to q_{comp} and will be much stiffer than a stress-strain path starting at the origin of the
569 axes.

570

571 Secondly, the stress field around the anchor was modified by the compressive crowd load, as
572 can be observed in Figure 14(c, d). Consequently, the strength and stiffness increased, as
573 they were a function of the average stress, as illustrated in Figure 11(b) and in the following
574 evolution of the unloading/reloading modulus E_{ur} definition

$$E_{ur}(p') = E_{ur}^{ref} \left(\frac{p'}{p_{ref}} \right)^m \quad (0)$$

575 where E_{ur}^{ref} is the reference modulus for $p_{ref}' = 100 \text{ kPa}$, p' is the average stress and m is a
576 material parameter. The consequence of these combined effects is a very complex pattern of
577 operative stiffness all around the anchor prior to uplift, as depicted in Figure 14(a, b).
578 However, it is clear that the stiffness above the anchor, in a zone delimited by the expected
579 failure mechanism (dashed line), was larger if the entire installation process was accounted
580 for (stage 2), rather than only the last recorded compression load (stage 1).

581

582 It should be noted that the installation simulation did not modify the shape of the failure
583 mechanism. Additional uplift simulations were run, incorporating the installation simulation,
584 but with no pre-defined mechanism. The observed failure mechanism was identical to that
585 from the stage 1 simulation.

586

587 ***Cylindrical failure mechanism***

588 Schiavon (2016) and Perez et al. (2018) recently investigated the disturbance effect around
589 screw anchors in centrifuge tests. The authors carried out micro-tomographic analyses of the
590 sand around the screw anchor and identified that the vertical soil column above the helix
591 was highly disturbed (lower density). They concluded that the failure mechanism should be a
592 vertical cylindrical failure whose section is identical to the area of the helix. This result is

593 consistent with experiments undertaken in calibration chambers (Nagata and Hirata 2005;
594 Nagai et al. 2018), which exhibit a cylindrical failure mechanism, although the pressurised
595 calibration chamber process impedes the development of any shallow failure mechanism. To
596 replicate this mechanism, Perez et al. (2018) introduced two cylindrical zones of soil in their
597 finite element simulations, whose properties were back-calculated to reproduce the
598 centrifuge tests. The friction angles leading to the best fit of the experimental results were
599 close to the critical state friction angle.

600 The cylindrical failure mechanism hypothesis has been tested in the following with or
601 without an installation process. Three scenarios incorporating a pre-defined cylindrical
602 failure mechanism, were compared with reference simulations for the U1VD-A case in Figure
603 16. The first simulation included a cylindrical failure mechanism using a reduced friction
604 angle ($\phi_r=40^\circ$), lying between the undisturbed peak and the critical state friction angle.
605 Results show that the load-displacement relationship was similar to the stage 1 simulation
606 where there is no pre-defined failure mechanism at all. This was corroborated by the
607 inspection of the failure mechanism (shear strain), which showed a conical pattern as before.
608 Two other simulations adopted the same cylindrical failure mechanism as per micro-
609 tomographic observations of Schiavon (2016) but used the critical state friction angle along
610 the cylindrical failure mechanism, which would be consistent with a highly disturbed zone of
611 soil. In this case, modelling the crowd-force installation effects, i.e. combining density and
612 stress installation disturbance, makes a significant difference to the capacity obtained
613 (Figure 16, with installation, 1MN, without, 5MN), but the maximum capacity is still lower
614 than both the reference simulation and the centrifuge results.

615 In summary, the centrifuge results obtained at the University of Dundee and presented in
616 (Davidson et al. 2019) are better approximated by a conical shallow failure mechanism while

617 a cylindrical failure mechanism gives a better approximation of the results for the numerical
618 simulations of Pérez et al. (2018). These two possibilities are not necessarily mutually
619 exclusive. Large geometries representative of the offshore requirements were used in this
620 study while Pérez et al. (2018) presented results for typical onshore piles, which are much
621 smaller. This difference in scale and in geometry (D_h/D_c ratio, tip shape) can lead to different
622 stress distribution or disturbance around the anchor and generate different failure
623 mechanism. In any case, the principal benefit of the new two-stage approach over that
624 proposed by Perez et al. (2018) is that there is no need to assume a priori empirically-
625 derived strength reduction factors as the final simulation is informed by directly measured
626 soil parameters, the results of the stage 1 WIP simulation and an explicit (though
627 approximate) simulation of the installation process. Further research is necessary to improve
628 the methodology proposed here, for instance by incorporating density variations resulting
629 from the installation process, i.e. the shaft and helix penetration.

630

631 ***Application in engineering design***

632 The two-stage simulation process presented herein can in principle be applied to any soil
633 profile and can provide the full load-displacement curve, allowing both uplift capacity and
634 stiffness at working load to be assessed. The process can be summarised by the following
635 steps:

636

- 637 1. Determine the crowd force required to install the screw anchor as a function of
638 depth, using a methodology previously developed (Davidson et al. 2018);
- 639 2. Conduct an uplift simulation (stage 1) of the screw anchor in the 'wished-in-place'
640 configuration;

- 641 3. Assess the shear band pattern from stage 1 output and the distance over which
642 softening should take place based on the induced shear stresses, with respect to
643 laboratory test results for the soil in question (e.g. direct shear test);
- 644 4. Modify the stage 1 model (from (2)) to include a multi-step press-replace procedure
645 (informed by predicted crowd forces from (1)) followed by the addition of soil-soil
646 interfaces with appropriate softening behaviour at the location of the shear bands
647 (from (3)) to the final (installed) anchor configuration;
- 648 5. Run the stage 2 model to determine the anchor performance (load-displacement
649 relationship).

650

651 It should be noted that this procedure has only been validated here for large dimension
652 screw anchors (representative of offshore applications) embedded in uniform deposits of
653 sand at a relatively shallow depth ($H/D_n \leq 8$). In such deposits, as a first approximation, the
654 process might be shortened by defining directly the failure mechanism as a shallow wedge
655 whose inclination to the vertical is equal to the dilatancy angle and defining the reduced
656 strength distance for the soil-soil interface based on Figure 15. This would have the effect of
657 removing stage 1. If the uplift capacity only is required (e.g. in initial Front-End Engineering
658 Design), the step preloading phase might also be neglected as a first approximation for single
659 helix anchors.

660

661 **CONCLUSION**

662 In this paper, a numerical methodology, based on the Finite Element (FE) method, has been
663 derived to enable predictions of the entire load-displacement relationship (including the
664 stiffness at working load and uplift capacity) of screw anchors embedded in sand. It meets a

665 need to provide improved prediction of uplift capacity (which is significantly overestimated
666 using existing analytical methods) identified from the literature, which is required for anchor
667 sizing, and additionally provides information on (non-linear) anchor axial stiffness which
668 controls the global rotational deformation of a jacket structure or tension-leg platforms. This
669 methodology is applicable in principle to any screw anchor geometry and ground conditions
670 and can be fully parametrised based on basic soil element testing and in-situ (CPT) tests in
671 sands. Installation-induced initial conditions within the soil can be approximated using
672 predicted crowd forces, based either on CPT data using a previously developed prediction
673 method, or from crowd force measurements taken from the installation records in the field.

674

675 The predictions of screw anchor tensile uplift performance were consistent with centrifuge
676 test results, with or without installation effects, that were previously published in the
677 literature. The FE analyses revealed that, as a significant vertical displacement is required to
678 fully form the failure mechanism, high induced shear strain along a part of the failure
679 mechanism close to the helix is such that critical state should be reached. The numerical
680 results also showed that the compression (crowd) load applied during the screw anchor
681 installation phase modifies the stress field around the anchor, which in turn affects the
682 anchor uplift stiffness.

683

684 The methodology developed in this paper, enables the prediction of uplift capacity (ultimate
685 limit state) and stiffness (serviceability limit state), accounting for installation effects in an
686 approximate way without empirical modifications to soil properties, and so can be used to
687 assess screw anchor performance using commercially available FE software. This approach
688 could lead to cost reduction, more reliable and efficient screw anchor design, enabling the

689 generalisation of this anchorage solution for applications in offshore geotechnical
690 engineering.

691

692 **ACKNOWLEDGEMENTS**

693 This project has received funding from the European Union's Horizon 2020 research and
694 innovation programme under the Marie Skłodowska-Curie grant agreement No 753156. The
695 authors would like to acknowledge the support of the Engineering and Physical Science
696 Research Council (EPSRC) (Grant no. EP/N006054/1: Supergen Wind Hub Grand Challenges
697 Project: Screw piles for wind energy foundations). The 5th author would like to acknowledge
698 the financial support of the Iraqi Ministry of higher Education of Scientific Research
699 (MOHESR). Elements of this work were undertaken using facilities developed as part of the
700 ERDF-funded Scottish Marine & Renewables Test Centre (SMART) at the University of
701 Dundee.

702

703

704 **SYMBOLS**

A	Helix area (including core area)
d_{50}	Is the size of particles such that 50% of the particles are smaller than this size.
D_c	Core diameter
D_h	Helix diameter
D_r	Relative density
E_{ur}, E_{ur}^{ref}	Unloading/reloading Young modulus and reference Young modulus respectively
FE	Finite element
F_y	Vertical load applied at the top of the screw anchor (positive in tension)
H	Helix embedment depth
I_R	Relative dilatancy index, (Bolton 1986)
m	Material parameter of the HSsmall model
MD	Medium-dense sand ($D_r = 57\%$, UoD test)
N_y	Non-dimensional uplift bearing factor
p	Average stress
p'_{ref}	Reference pressure for the determination of stress dependent stiffness in the HSsmall model

u_y	Vertical displacement measured at the top of the screw anchor
VD	Very-dense sand ($D_r = 84\%$, UoD test)
γ'	Buoyant unit weight
γ_s	Shear strain
$\gamma_{s,th}$	Threshold of shear strain at which critical state is supposed to be reached
$\Delta\gamma_s$	Increment of shear strain over a time step
Δu_y	Increment of vertical displacement of a time step
θ	Inclination to the vertical direction of the theoretical straight failure plane emanating from the anchor edge
ξ	Normalised distance from the edge of the anchor along the direction of the theoretical straight failure plane
σ'_h	Horizontal effective stress within the soil
σ'_N	Normal effective stress along any cross-section within the soil
$\sigma'_{N,G}$	Normal effective stress along the theoretical failure plane according to (Giampa et al. 2017)
τ	Shear stress along any cross-section within the soil
τ_G	Shear stress along the theoretical failure plane according to (Giampa et al. 2017)
τ_{rel}	Mobilised shear stress, ratio of the current to maximum shear stress
ϕ'_{cv}	Critical state friction angle
ϕ'_{pk}	Peak friction angle
ϕ'_r	Residual friction angle
ψ'_{pk}	Peak dilation angle

705

706

707 REFERENCES

- 708 Achmus, M., Kuo, Y.-S.S., and Abdel-Rahman, K. 2009. Behavior of monopile foundations under cyclic
709 lateral load. *Computers and Geotechnics*, **36**(5): 725–735. doi:10.1016/j.compgeo.2008.12.003.
- 710 Al-Baghdadi, T. 2018. Screw piles as offshore foundations : Numerical and physical modelling. PhD
711 Thesis, University of Dundee, UK.
- 712 Al-Baghdadi, T.A., Brown, M.J., Knappett, J.A., and Al-Defae, A.H. 2017a. Geotechnical engineering
713 effects of vertical loading on lateral screw pile performance. *Proceedings of the Institution of
714 Civil Engineers: Geotechnical Engineering*, **170**(3): 259–272. doi:10.1680/jgeen.16.00114.
- 715 Al-Baghdadi, T.A., Davidson, C., Brown, M.J., Knappett, J.A., Brennan, A., Augarde, C., Coombs, W.,
716 and Wang, L. 2017b. CPT based design procedure for installation torque prediction for screw
717 piles installed in sand. 8th International Conference on Offshore Site Investigation &
718 Geotechnics, (1): 346–353. Society for Underwater Technology, London, UK.
- 719 Al-Defae, A.H.H., Caucis, K., and Knappett, J.A.A. 2013. Aftershocks and the whole-life seismic
720 performance of granular slopes. *Géotechnique*, **63**(14): 1230–1244. Thomas Telford Ltd.

- 721 doi:10.1680/geot.12.P.149.
- 722 Anastasopoulos, I., Gazetas, G., Asce, M., Bransby, M.F., Davies, M.C.R., and Nahas, a El. 2007. Fault
723 Rupture Propagation through Sand : Finite-Element. *Journal of Geotechnical and*
724 *Geoenvironmental Engineering*, **133**(August): 943–958. doi:10.1061/(ASCE)1090-
725 0241(2007)133:8(943).
- 726 Bachynski, E.E., and Moan, T. 2014. Ringing loads on tension leg platform wind turbines. *Ocean*
727 *Engineering*, **84**: 237–248. Elsevier. doi:10.1016/j.oceaneng.2014.04.007.
- 728 Bailey, H., Senior, B., Simmons, D., Rusin, J., Picken, G., and Thompson, P.M. 2010. Assessing
729 underwater noise levels during pile-driving at an offshore windfarm and its potential effects on
730 marine mammals. *Marine Pollution Bulletin*, **60**(6): 888–897.
731 doi:10.1016/j.marpolbul.2010.01.003.
- 732 Bolton, M.D. 1986. The strength and dilatancy of sands. *Géotechnique*, **36**(1): 65–78.
- 733 Byrne, B.W., and Houlsby, G.T. 2015. Helical piles: an innovative foundation design option for
734 offshore wind turbines. *Philosophical Transactions of the Royal Society A: Mathematical,*
735 *Physical & Engineering Sciences*, **373**(February): 1–11. doi:10.1098/rsta.2014.0081.
- 736 Cerfontaine, B., Knappett, J.A., Brown, M.J., and Bradshaw, A.S. 2019. Effect of soil deformability on
737 the failure mechanism of shallow plate or screw anchors in sand. *Computers and Geotechnics*,
738 **109**(May): 34–45. doi:https://doi.org/10.1016/j.compgeo.2019.01.007.
- 739 Das, B.M., and Shukla, S.K. 2013. *Earth anchors*. J. Ross, Plantation, Florida.
- 740 Davidson, C., Al-Baghdadi, T., Brown, M., Brennan, A., Knappett, J., Augarde, C., W., C., Wang, L.,
741 Richards, D., Blake, A., and Ball, J. 2018. A modified CPT based installation torque prediction for
742 large screw piles in sand. *In Cone Penetration Testing. Edited by M. Hicks, F. Pisanò, and J.*
743 *Peuchen*. Delft, The Netherlands.
- 744 Davidson, C., Brown, M.J., Brennan, A.J., Knappett, J.A., Cerfontaine, B., and Sharif, Y.U. 2019.
745 Physical modelling of screw piles for offshore wind energy. *In First International Symposium on*
746 *Screw Piles for Energy Applications. Edited by C. Davidson, M.J. Brown, J.A. Knappett, A.J.*
747 *Brennan, C. Augarde, W. Coombs, L. Wang, D. Richards, D.J. White, and A. Blake*. University of
748 Dundee, Dundee, UK.
- 749 Davidson, C., Brown, M.J., Cerfontaine, B., Al-Baghdadi, T., Knappett, J., Brennan, A., Augarde, C.,
750 Coombs, W., Wang, L., Blake, A., Richards, D., and Ball, J. 2020. Physical modelling to
751 demonstrate the feasibility of screw piles for offshore jacket supported wind energy structures.

- 752 (submitted for consideration in) *Géotechnique*,.
- 753 Desrues, J., and Viggiani, G. 2004. Strain localization in sand: an overview of the experimental results
754 obtained in Grenoble using stereophotogrammetry. *International Journal for Numerical and*
755 *Analytical Methods in Geomechanics*, **28**(4): 279–321. doi:10.1002/nag.338.
- 756 Dickin, E.A. 1988. Uplift behaviour of horizontal anchor plates in sand. *Journal of Geotechnical and*
757 *Geoenvironmental Engineering*, **114**(11): 1300–1317.
- 758 Engin, H.K., Brinkgreve, R.B.J., and van Tol, A.F. 2015. Simplified numerical modelling of pile
759 penetration - the press-replace technique. *International Journal for Numerical and Analytical*
760 *Methods in Geomechanics*, **39**(March): 1713–1734. doi:10.1002/nag.2736.
- 761 Garnier, J., Gaudin, C., Springman, S.M., Culligan, P.J., Goodings, D., König, D., Kutter, B., Phillips, R.,
762 Randolph, M.F., Thorel, A., Garnier, J., Gaudin, C., Springman, S.M., Culligan, P.J., Goodings, D.,
763 König, D., Kutter, B., Phillips, R., Randolph, M.F., and Thorel, L. 2007. Catalogue of scaling laws
764 and similitude questions in geotechnical centrifuge modelling. *International Journal of Physical*
765 *Modelling in Geotechnics*, **7**(3): 01–23. doi:10.1680/ijpmg.2007.070301.
- 766 Gavin, K., Doherty, P., and Tolooiyan, A. 2014. Field investigation of the axial resistance of helical
767 piles in dense sand. *Canadian Geotechnical Journal*, **51**(11): 1343–1354. doi:10.1139/cgj-2012-
768 0463.
- 769 Ghaly, A., Hanna, A., and Hanna, M. 1991. Uplift behaviour of screw anchor in sand, I dry sand.
770 *Journal of Geotechnical Engineering*, **117**(5): 773–793.
- 771 Giampa, J., Bradshaw, A., and Schneider, J. 2017. Influence of Dilation Angle on Drained Shallow
772 Circular Anchor Uplift Capacity. *International Journal of Geomechanics*, **17**(2): 4016056.
773 doi:10.1061/(ASCE)GM.1943-5622.0000725.
- 774 Giampa, J.R., Bradshaw, A., Gerkus, H., Gilbert, R.B., Gavin, K.G., and Sivakumar, V. 2018a. The effect
775 of shape on the pullout capacity of shallow plate anchors in sand. *Géotechnique*,.
- 776 Giampa, J.R., Bradshaw, A.S., and Schneider, J.A. 2018b. Erratum for “Influence of Dilation Angle on
777 Drained Shallow Circular Anchor Uplift Capacity” by Joseph R. Giampa, Aaron S. Bradshaw, and
778 James A. Schneider. *International Journal of Geomechanics*, **18**(11): 08218002.
779 doi:10.1061/(asce)gm.1943-5622.0001329.
- 780 Gudehus, G., and Nübel, K. 2004. Evolution of shear bands in sand. *Géotechnique*, **54**(3): 187–201.
781 doi:10.1680/geot.54.3.187.36346.

- 782 Hao, D., Wang, D., O'Loughlin, C.D., Gaudin, C., O'Loughlin, C.D.C.D., and Gaudin, C. 2018. Tensile
783 monotonic capacity of helical anchors in sand: interaction between helices. *Canadian*
784 *Geotechnical Journal* (in press),. doi:10.1139/cgj-2018-0202.
- 785 Houlsby, G.T. 2016. Interactions in offshore foundation design. *Géotechnique*, **66**(10): 791–825.
786 doi:10.1680/jgeot.15.RL.001.
- 787 Ilamparuthi, K., Dickin, E.A., and Muthukrisnaiah, K. 2002. Experimental investigation of the uplift
788 behaviour of circular plate anchors embedded in sand. *Canadian Geotechnical Journal*, **39**: 648–
789 664. doi:10.1139/t02-005.
- 790 Ilamparuthi, K., and Muthukrishnaiah, K. 1999. Anchors in sand bed: Delineation of rupture surface.
791 *Ocean Engineering*, **26**(12): 1249–1273. doi:10.1016/S0029-8018(98)00034-1.
- 792 Jaky, J. 1944. The coefficient of earth pressure at rest. *Journal of the Society of Hungarian Architects*
793 *and Engineers*, **78**(5): 355–358.
- 794 Klinkvort, R.F., Hededal, O., and Springman, S.M. 2013. Scaling issues in centrifuge modelling of
795 monopiles. *International Journal of Physical Modelling in Geotechnics*, **13**(2): 38–49. doi:http://
796 dx.doi.org/10.1680/ijpmg.12.00010.
- 797 Knappett, J.A., Brown, M.J., Brennan, A.J., and Hamilton, L. 2014. Optimising the compressive
798 behaviour of screw piles in sand for marine renewable energy applications. *In International*
799 *Conference on Piling and Deep foundations*. Stockholm, Sweden.
- 800 Knappett, J.A., Caucis, K., Brown, M.J., Jeffrey, J.R., and Ball, J.D. 2016. CHD pile performance: part II –
801 numerical modelling. *Proceedings of the Institution of Civil Engineers - Geotechnical*
802 *Engineering*, **169**(5): 436–454. doi:10.1680/jgeen.15.00132.
- 803 Lauder, K.D., Brown, M.J., Bransby, M.F., and Boyes, S. 2013. The influence of incorporating a
804 forecutter on the performance of offshore pipeline ploughs. *Applied Ocean Research*, **39**: 121–
805 130. Elsevier Ltd. doi:10.1016/j.apor.2012.11.001.
- 806 Lauder, K.D., Brown, M.J., Bransby, M.F., and Gooding, S. 2012. Variation of tow force with velocity
807 during offshore ploughing in granular materials. *Canadian Geotechnical Journal*, **49**(11): 1244–
808 1255. doi:10.1139/t2012-086.
- 809 Li, Z., Haigh, S.K., and Bolton, M.D. 2010. Centrifuge modelling of mono-pile under cyclic lateral loads.
810 *Proceedings of the 7th International Conference on Physical Modelling in Geotechnics*, **2**: 965–
811 970. doi:10.1680/ijpmg.2010.10.2.47.

- 812 Liu, J.Y., Liu, M.L., and Zhu, Z.D. 2012. Sand Deformation around an Uplift Plate Anchor. *Journal of*
813 *Geotechnical and Geoenvironmental Engineering*, **138**(6): 728–737. doi:Doi
814 10.1061/(Asce)Gt.1943-5606.0000633.
- 815 Livneh, B., and El Naggar, M.H. 2008. Axial testing and numerical modeling of square shaft helical
816 piles under compressive and tensile loading. *Canadian Geotechnical Journal*, **45**: 1142–1155.
817 doi:10.1139/T08-044.
- 818 Meyerhof, G.G., and Adams, J.I. 1968. The ultimate uplift capacity of foundations. *Canadian*
819 *Geotechnical Journal*, **5**(4): 225–244.
- 820 Mitsch, M.P., and Clemence, S.. 1985. The uplift capacity of helix anchors in sand. *In Uplift behavior*
821 *of anchor foundations in soil*. Proceedings of the ASCE. New-York, USA. pp. 26–47.
- 822 Mosquera, Z.S.Z., Tsuha, H.C., Schiavon, J.A., and Thorel, L. 2015. Discussion of Field investigation of
823 the axial resistance of helical piles in dense sand. *Canadian Geotechnical Journal*, **52**(11): 1190–
824 1194. doi:10.1139/cgj-2012-0463.
- 825 Nagai, H., Tsuchiya, T., and Shimada, M. 2018. Influence of installation method on performance of
826 screwed pile and evaluation of pulling resistance. *Soils and Foundations*, **58**(2): 355–369.
827 Elsevier B.V. doi:10.1016/j.sandf.2018.02.006.
- 828 Nagata, M., and Hirata, H. 2005. Study on Uplift Resistance of Screwed Steel Pile. (92): 73–78.
- 829 Newgard, J.T., Schneider, J. a., and Thompson, D.J. 2015. Cyclic response of shallow helical anchors in
830 a medium dense sand. *In Frontiers in Offshore Geotechnics III*. Taylor & Francis Group, London,
831 Oslo, Norway. pp. 913–918.
- 832 Papadopoulou, K., Saroglou, H., and Papadopoulos, V. 2014. Finite Element Analyses and
833 Experimental Investigation of Helical Micropiles. *Geotechnical and Geological Engineering*,
834 **32**(4): 949–963. doi:10.1007/s10706-014-9771-6.
- 835 Pérez, Z.A., Schiavon, J.A., Tsuha, C.H.C., Dias, D., and Thorel, L. 2018. Numerical and experimental
836 study on the influence of installation effects on the behaviour of helical anchors in very dense
837 sand. *Canadian Geotechnical Journal*, **55**(8): 1067–1080. doi:10.1139/cgj-2017-0137.
- 838 Perko, H.A. 2000. Energy method for predicting installation torque of helical foundations and
839 anchors. *ASCE Geotechnical Special Publication*,: 1–11. doi:10.1061/40511(288)24.
- 840 Perko, H.A. 2009. *Helical Piles: A Practical Guide to Design and Installation*. *In 1st Edit*. John Wiley &
841 Sons.

- 842 PLAXIS. 2017a. PLAXIS 2D Reference Manual. Delft, The Netherlands.
- 843 PLAXIS. 2017b. PLAXIS Material Models Manual. Delft, The Netherlands.
- 844 Robinson, S. 2016. Internal report for project Seabed Ploughing : Modelling for Infrastructure
845 EP/M000362/1. Dundee, UK.
- 846 Schanz, T. 1998. Zur Modellierung des Mechanischen verhaltens von Reibungsmaterialien. Universität
847 Stuttgart, Germany.
- 848 Schanz, T., Vermeer, A., and Bonnier, P. 1999a. The hardening soil model: formulation and
849 verification. *In* Beyond 2000 Comput. Geotech. 10 years PLAXIS. Amsterdam, The Netherlands.
850 pp. 281–296.
- 851 Schanz, T., Vermeer, A., and Bonnier, P. 1999b. The hardening soil model: formulation and
852 verification. *Beyond 2000 Comput. Geotech. 10 years PLAXIS Int. Proc. Int. Symp. beyond 2000*
853 *Comput. Geotech. Amsterdam Netherlands 1820 March 1999,:* 281.
- 854 Schanz, T., and Vermeer, P.A. 1996. Angles of friction and dilatancy of sand. *Géotechnique*, **46**(1):
855 145–151.
- 856 Schiavon, J.A. 2016. Comportamento de ancoragens helicoidais submetidas a carregamentos cíclicos.
857 PhD Thesis. University of São Paulo, Brazil.
- 858 Sharif, Y.U., Brown, M.J., Ciantia, M.O., Knappett, J.A., Davidson, C., Cerfontaine, B., and Robinson, S.
859 2019. Numerically modelling the installation and loading of screw piles using DEM. *In*
860 *Proceedings of the International Symposium on Screw Piles for Energy Applications. Dundee,*
861 *UK.*
- 862 Sutherland, H.B. 1965. Model Studies for Shaft Raising through Cohesionless Soils. *In* *Proceedings of*
863 *the 6th International Conference on Soil Mechanics and Foundation Engineering, Montréal.*
864 *Montreal, Canada. pp. 410–413.*
- 865 Tappenden, K.M. 2007. Predicting the axial capacity of screw piles installed in Canadian soils. Msc
866 Thesis, University of Alberta.
- 867 Tsuha, C.H.C., Aoki, N., Rault, G., Thorel, L., and Garnier, J. 2007. Physical modelling of helical pile
868 anchors. *International Journal of Physical Modelling in Geotechnics*, **49**(4): 1–12.
- 869 Tsuha, C.H.C., Aoki, N., Rault, G., Thorel, L., and Garnier, J. 2012. Evaluation of the efficiencies of
870 helical anchor plates in sand by centrifuge model tests. *Canadian Geotechnical Journal*, **49**(9):
871 1102–1114. doi:Doi 10.1139/T2012-064.

- 872 Tucker, K.. 1987. Uplift capacity of drilled shafts and driven piles in granular materials. *In Foundations*
873 for transmission line towers. pp. 142–159.
- 874 Vermeer, P.A., and Sutjiadi, W. 1985. The uplift resistance of shallow embedded anchors. *In Proc.*, of
875 11th Int. Conf. of Soil Mechanics and Foundation Engineering. Balkema, Rotterdam, The
876 Netherlands, San Francisco, USA. pp. 1635–1638.
- 877 Wang, L., Coombs, W.M., Augarde, C.E., Brown, M., Knappett, J., Brennan, A., Richards, D., and Blake,
878 A. 2017. Modelling Screwpile Installation Using the MPM. *Procedia Engineering*, **175**: 124–132.
879 Elsevier B.V. doi:10.1016/j.proeng.2017.01.040.
- 880 White, D.J., Cheuk, C.Y., and Bolton, M.D. 2008. The uplift resistance of pipes and plate anchors
881 buried in sand. *Géotechnique*, **58**(10): 771–779. doi:10.1680/geot.2008.3692.
- 882 Zienkiewicz, O.C., and Taylor, R.L. 2000. The finite element method (vol. 2): Solid mechanics. *In Vasa*,
883 Fifth Edit. Butterworth-Heinemann, Oxford, UK.
- 884

885 **FIGURE CAPTION LIST**

- 886 Figure 1 Comparison of centrifuge tests with respect to relatively large scale 1g, centrifuge and field
887 experimental results, for plate anchors (wished in place, open markers) and screw anchors
888 (installation effect, closed markers). Centrifuge and field tests are underlined by solid and dashed
889 lines respectively. Single and double refer to the number of helices. The Giampa et al. (2017)
890 criterion is calculated for very dense (VD) and medium-dense (MD) soil properties.
- 891 Figure 2 Schematic description of the multi-stage methodology
- 892 Figure 3 Comparison of the load-displacement relationship for the wished in place centrifuge tests
893 ($H/D_h = 6$) in dense sand from (Hao et al. 2018) and numerical simulations (Stage 1 & Stage 2 -
894 capacity)
- 895 Figure 4 Comparison of wished in place centrifuge tests in dense sand from (Hao et al. 2018) and
896 numerical simulations (Stage 2 - capacity). The two sets of parameters used to calculate the
897 analytical criterion of Giampa et al. (2017) correspond to the maximum and minimum density values.
- 898 Figure 5 Comparison of centrifuge test results and finite element simulations (stages 1 & 2). (a)
899 U1VD-A, $H/D_h = 5.9$; (b) U1MD, $H/D_h = 4.5$; (c) U1VD-B, $H/D_h = 7.4$; (d) U2VD, $H/D_{h,1} = 7.4$ & $H/D_{h,2} = 5.4$

900 Figure 6 Failure mechanism development at different anchor imposed displacements ($u_{y,imposed}$), single
901 helix in very dense sand (U1VD-B, $H/D_h = 7.4$), the dashed line indicates the failure mechanism
902 assumed by (Giampa et al. 2017).

903 Figure 7 Failure mechanism development at different anchor imposed displacements ($u_{y,imposed}$),
904 double helix in very dense sand (U2VD, $H/D_h=7.4\& 5.4$), the inclined dashed line indicates the failure
905 mechanism assumed by (Giampa et al. 2017).

906 Figure 8 Comparison of the indicators of failure at the anchor's head ($u_{y,imposed}$), (U1VD-B) and soil-soil
907 interface, the dashed line indicates the soil-soil interface

908 Figure 9 Consideration of cross-section along the assumed failure mechanism for the single helix
909 embedded in very dense sand (U1VD-B), ξ is the distance from the edge of the plate in the direction
910 of the cross-section, τ_{max} is the maximum shear stress that could be mobilised ($=\sigma'_N \tan \phi' pk$).

911 Figure 10 Comparison of the stress distribution along a cross-section (inclined at ψ degrees to the
912 vertical) and along the interface elements for the single helix (U1VD-B), after a vertical displacement
913 $u_y = 0.3D_h$

914 Figure 11 Consideration of the cross-section along the assumed mechanism ($\psi = 17^\circ$) for a single
915 helix screw anchor ($D_h = 1.7m$) embedded at different depths in very dense (VD) sand, stage 1
916 simulations, ξ is the distance from the edge of the plate in the direction of the cross-section, τ_{max} is
917 the maximum shear stress that could be mobilised ($=\sigma'_N \tan \phi' pk$).

918 Figure 12 Normalised distance along the failure plane over which the shear strain γ_s is larger or equal
919 to 10% with respect to normalised plate depth

920 Figure 13 Comparison of bearing factors N_y for a single helix screw anchor ($D_h = 1.7m$) at two
921 different densities and stage 2 (enhanced capacity). (a) $D_r = 57\%$; (b) $D_r = 84\%$.

922 Figure 14 Comparison of unloading/reloading Young modulus E_{ur} (a-b) and effective average stress p'
923 (c-d) after a step-installation procedure (a, c) or after a single compression load (b, d). The inclined
924 dashed line indicates the soil-soil interface position in stage 2.

925 Figure 15 Idealisation of the installation effect on the soil behaviour, based on the small-strain
926 Hardening soil model. (a) Effect of previous shearing; (b) Effect of average stress increase.

927 Figure 16 Comparison of centrifuge (U1VD-A, $H/D_h = 5.9$) and numerical solutions with different
928 imposed failure mechanisms.

929

930

931 **TABLE CAPTION LIST**

932 Table 1 Geometry, crowd force ($F_{y,min}$) and uplift capacity (F_y) of the different screw pile models at
933 prototype scale for UoD (Davidson et al. 2019) and UWA (Hao et al. 2018) tests

934 Table 2 Properties of the plate elements (identical for pile core and helices), assumed identical for all
935 tests

936 Table 3 Number of elements and nodes of the meshes for each simulation (stage 1)

937 Table 4 HSsmall parameters for the HST95 Congleton sand, after (Al-Defae et al. 2013, Lauder et al.
938 2013, Al-Baghdadi et al. 2017a), reference stiffness is for a reference pressure $p^{ref} = 100kPa$.

939 Table 4 Comparison of the uplift capacity and CPU run time as a function of the mesh refinement for
940 the U1VD-B. The CPU time is normalised with respect to the fastest simulation (mesh #1)

941 Table 6 Effect of the preloading level ($F_{y0,max}$) on the uplift capacity (F_y) of the single deep helix (U1VD-
942 B,)

943 Table 7 Comparison of the pitch to helix diameter ratio for different studies

944

945

946 **TABLES**

947 Table 1 Geometry, crowd force ($F_{y,min}$) and uplift capacity (F_y) of the different screw pile models at
 948 prototype scale for UoD (after Davidson et al. 2019) and UWA (after Hao et al. 2018) tests

	Helix numbe r	D_r [%]	D_h [m]	D_s [m]	H [m]	H/ D_h	Pitch [m]	$F_{y,min}$ [MN]	F_y [MN]
UoD tests									
U1VD-A	1	84	1.7	0.88	10	5.9	0.56	-12.5	6.4
U1VD-B	1	84	1.7	0.88	12.5	7.4	0.56	-18.0	10.6
U2VD	2	84	1.7	0.88	9.1/12. 5	5.4/7. 4	0.56	-20.2	10.8
U1MD	1	57	3.4	1.13	15.2	4.5	0.56	-21.0	15
UWA tests									
SP3	1	85.8	0.4	0.094	1.2	3	0.1	Wished-in-Place	0.023
SP6	1	85.8	0.4	0.094	2.4	6	0.1		0.109
SP9	1	85.8	0.4	0.094	3.6	9	0.1		0.236
SP12-a	1	85.5	0.4	0.094	4.8	12	0.1		0.358
SP12-b	1	85.4	0.4	0.094	4.8	12	0.1		0.313
SH2	1	86.7	0.4	0.094	0.8	2	0.1		0.001
SH3-a	1	86.4	0.4	0.094	1.2	3	0.1		0.022
SH3-b	1	96.2	0.4	0.094	1.2	3	0.1		0.023
SH4	1	86.7	0.4	0.094	1.6	4	0.1		0.043
SH6-a	1	86.4	0.4	0.094	2.4	6	0.1		0.108
SH6-c	1	96.2	0.4	0.094	2.4	6	0.1		0.122
SH7.5	1	90.0	0.4	0.094	3.0	7.5	0.1		0.162
SH8-a	1	86.4	0.4	0.094	3.2	8	0.1		0.176
SH8-b	1	96.4	0.4	0.094	3.2	8	0.1		0.218
SH9-a	1	88.8	0.4	0.094	3.6	9	0.1		0.250
SH9-b	1	96.1	0.4	0.094	3.6	9	0.1		0.270
SH9-c	1	96.2	0.4	0.094	3.6	9	0.1		0.260
SH10	1	96.4	0.4	0.094	4.0	10	0.1		0.310
SH10.5	1	90.0	0.4	0.094	4.0	10.5	0.1		0.272
SH12-a	1	85.4	0.4	0.094	4.8	12	0.1		0.322
SH12-b		91.7	0.4	0.094	4.8	12	0.1	0.365	

949

950

951 Table 2 Properties of the plate elements (identical for pile core and helices), assumed identical for all
952 tests

EA	EI	t_{equiv}	ν
[GN/m]	[MNm ² /m]	[m]	[-]
38.08	39.8	0.112	0.3

953

954

955

956

957

958

959 Table 3 Number of elements and nodes of the meshes for each simulation (stage 1). The minimum
 960 element size was normalised with respect to the helix diameter D_h .

		Elements	Min El. Size/ D_h [-]	Nodes
UoD	U1VD-A	2534	0.03	21206
	U1VD-B	3175	0.04	26476
	U2VD	3779	0.03	31428
	U1MD	3674	0.03	30296
UWA	SH2	3888	0.05	31770
	SH4	3514	0.05	28918
	SH6	4517	0.05	37128
	SH7.5	6382	0.05	52002
	SH9	5187	0.05	42448

961

962

963

964 Table 4 HSsmall parameters for the HST95 Congleton sand, after (after Lauder et al. 2013; Al-Defae
 965 et al. 2013; Al-Baghdadi et al. 2017a), reference stiffness is for a reference pressure $p^{ref} = 100\text{kPa}$.

Soil parameters		Unit	Equation	$D_r = 57\%$	$D_r = 84\%$
Min. void ratio	e_{min}	[-]		0.469	0.469
Max. void ratio	e_{max}	[-]		0.769	0.769
Initial void ratio	e_0	[-]		0.597	0.515
Peak friction angle	ϕ'_{pk}	[°]	$20 I_D + 29$	40.4	45.8
Dilatancy angle	ψ	[°]	$25 I_D - 4$	10.25	17
Effective apparent cohesion	c'	[kPa]	$25 I_D + 20.22$	1.0	1.0
Oedometer stiffness	E_{oed}^{ref}	[MPa]	$25 I_D + 20.22$	34.5	41.2
Secant stiffness	E_{50}^{ref}	[MPa]	$1.25 E_{oed}^{ref}$	43.1	51.5
Unloading/reloading stiffness	E_{ur}^{ref}	[MPa]	$3 E_{oed}^{ref}$	103.4	123.7
Material parameter	M	[-]	$0.6 - 0.1 I_D$	0.54	0.52
Unloading/reloading Poisson's ratio	ν_{ur}	[-]		0.2	0.2
Reference shear strain	$\gamma_{0.7}$	[-]	$(1.7 I_D + 0.67) \cdot 10^{-4}$	$1.64 \cdot 10^{-4}$	$2.09 \cdot 10^{-4}$
Low strain shear modulus	G_0^{ref}	[MPa]	$50 I_D + 88.8$	118.8	130.8
Total unit weight	γ_{tot}	[kN/m ³]	$30 I_D + 14.5$	19.83	20.30

966

967

968 Table 5 Comparison of the uplift capacity and CPU run time as a function of the mesh refinement for
 969 the U1VD-B (stage 1 simulation). The CPU time is normalised with respect to the fastest simulation
 970 (mesh #1). The average, maximum and minimum element sizes were normalised with respect to the
 971 helix diameter. The computer used had the following specifications: Intel® Xeon® CPU E5-1650 v4
 972 @3.60GHz, 24GB RAM, 64-bit operating system.

Mesh		1	2	3	4	5
Elements	[-]	498	808	2175	3175	5678
Average El. size/ D_h	[-]	0.94	0.73	0.37	0.29	0.22
Max El. Size/ D_h	[-]	3.75	2.75	2.08	2.61	1.91
Min El. Size/ D_h	[-]	0.15	0.11	0.04	0.04	0.03
Nodes	[-]	4337	6878	18292	26746	46866
$F_{y,0.1D_h}$	[MN]	13.78	12.95	13.64	13.35	13.13
$F_{y,max}$	[MN]	14	14.83	14.58	15.09	15.23
Normalised CPU time	[s]	1	3.4	19.2	24.4	46.7

973

974

975 Table 6 Effect of the preloading level ($F_{y0,max}$) on the uplift capacity (F_y) of the single deep helix (U1VD-
976 B)

$F_{y0,max}$ [MN]	F_y [MN]
-9	10.9
-18	11.3
-27	12.1

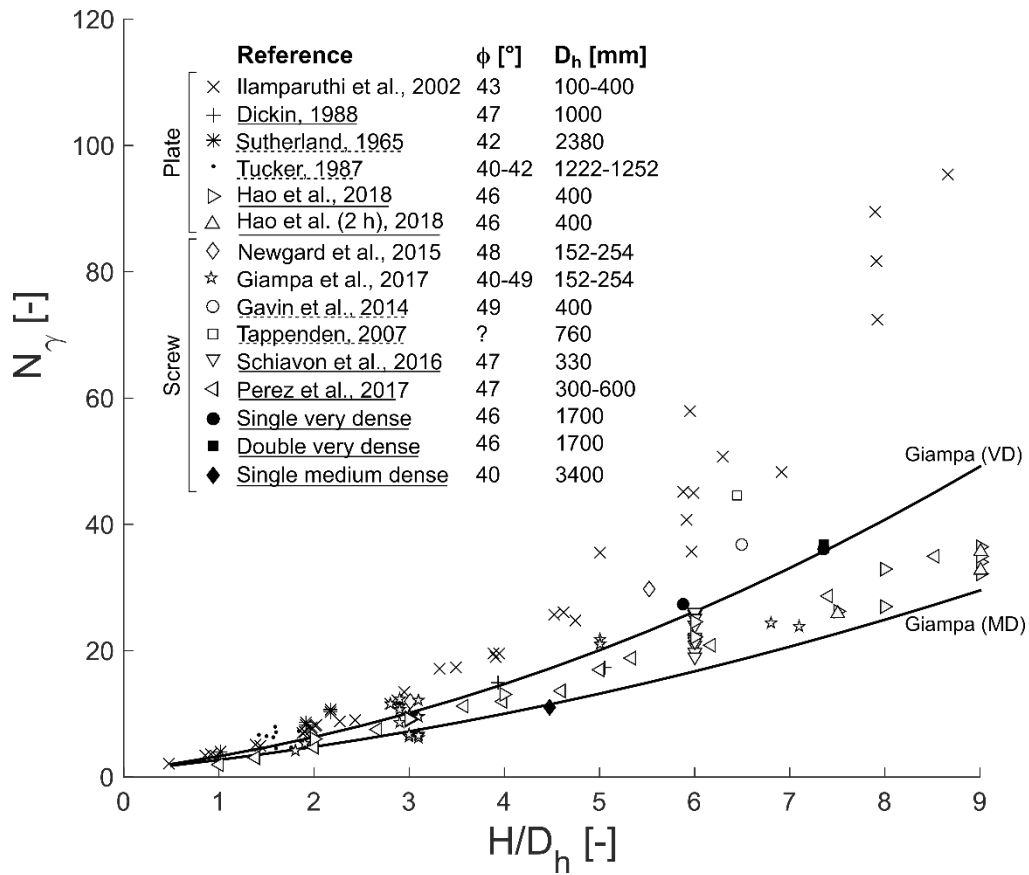
977

978

979

980 **FIGURES**

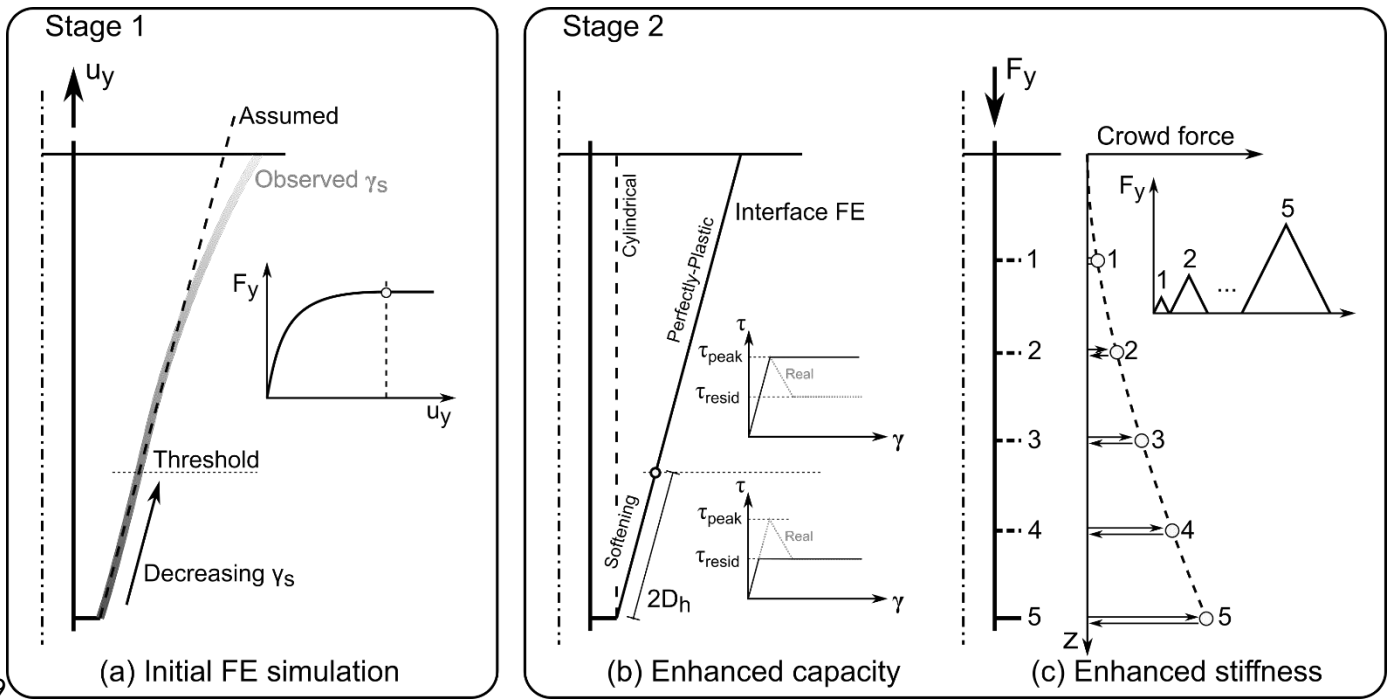
981



982

983 Figure 1 Comparison of centrifuge tests with respect to relatively large scale 1g, centrifuge and field
 984 experimental results, for plate anchors (wished in place, open markers) and screw anchors
 985 (installation effect, closed markers). Centrifuge and field tests are underlined by solid and dashed
 986 lines respectively. Single and double refer to the number of helices. The Giampa et al. (2017)
 987 criterion is calculated for very dense (VD) and medium-dense (MD) soil properties.

988

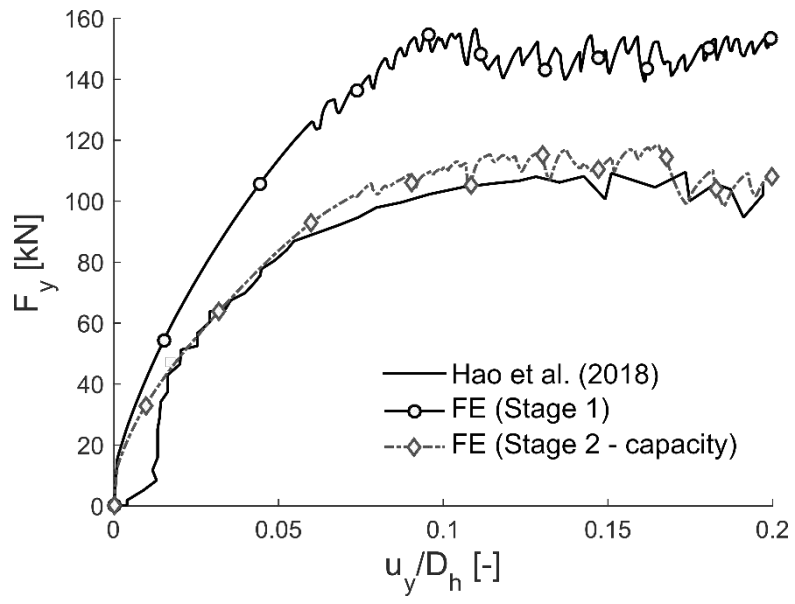


989

990 Figure 2 Schematic description of the multi-stage methodology

991

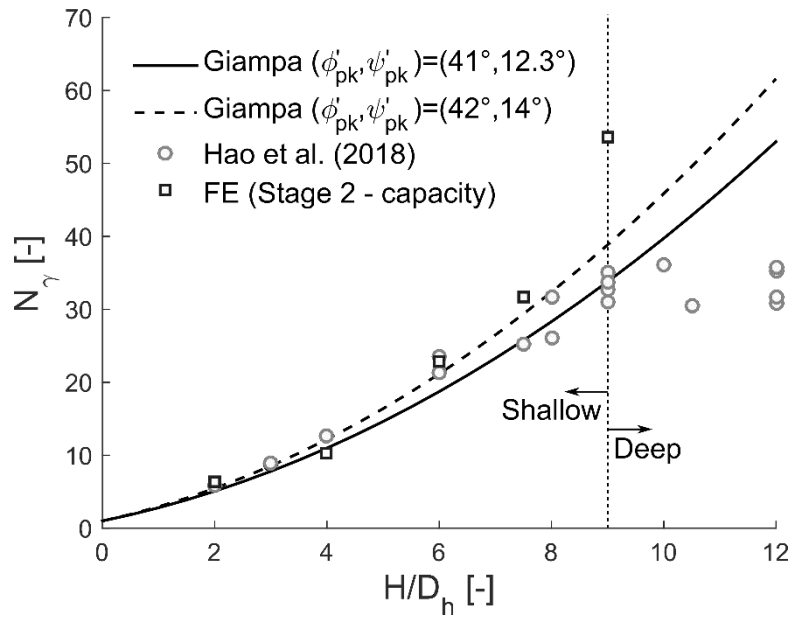
992



993

994 Figure 3 Comparison of the load-displacement relationship for the wished in place centrifuge tests
995 ($H/D_h = 6$) in dense sand from Hao et al. (2018) and numerical simulations (Stage 1 & Stage 2 -
996 capacity)

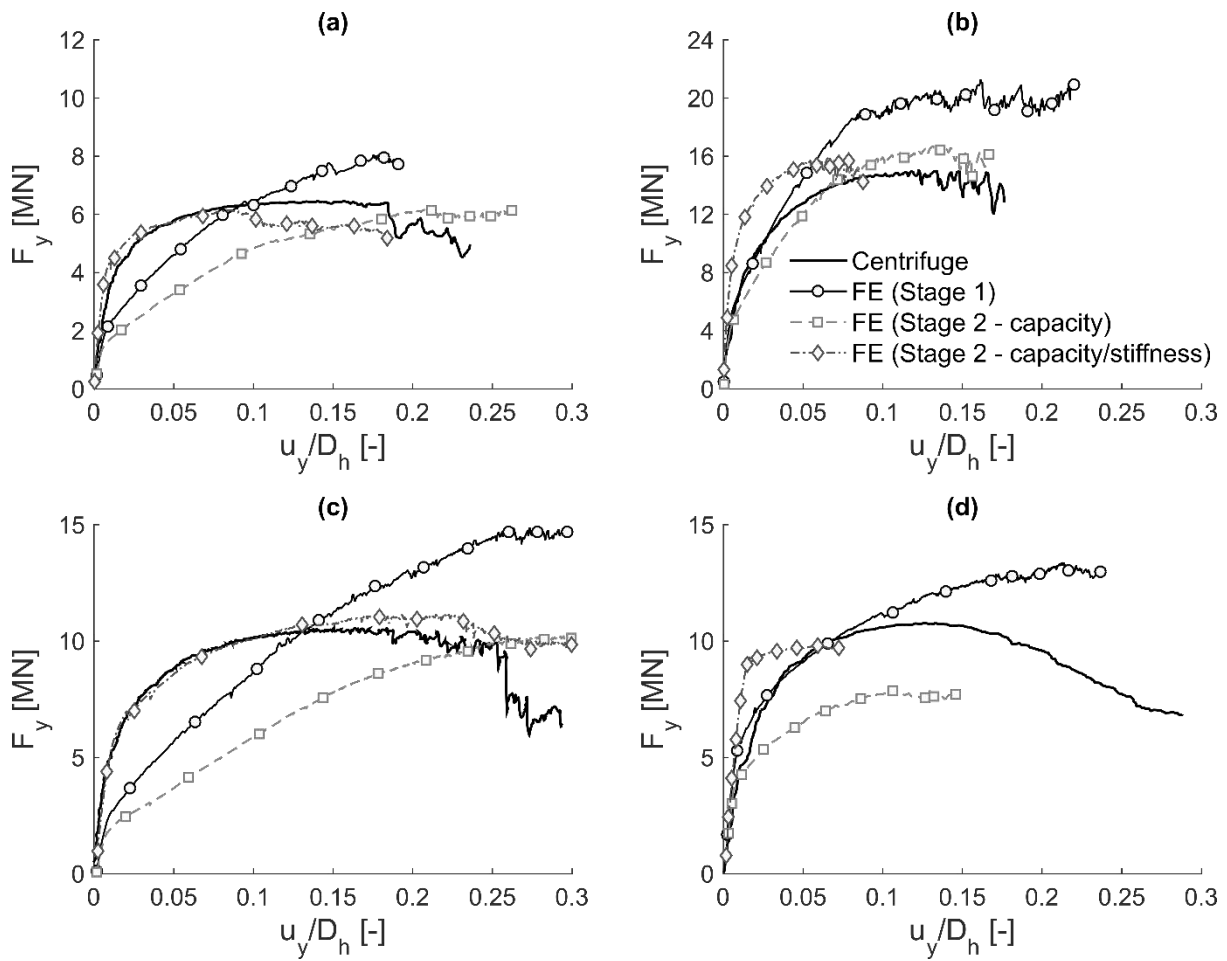
997



998

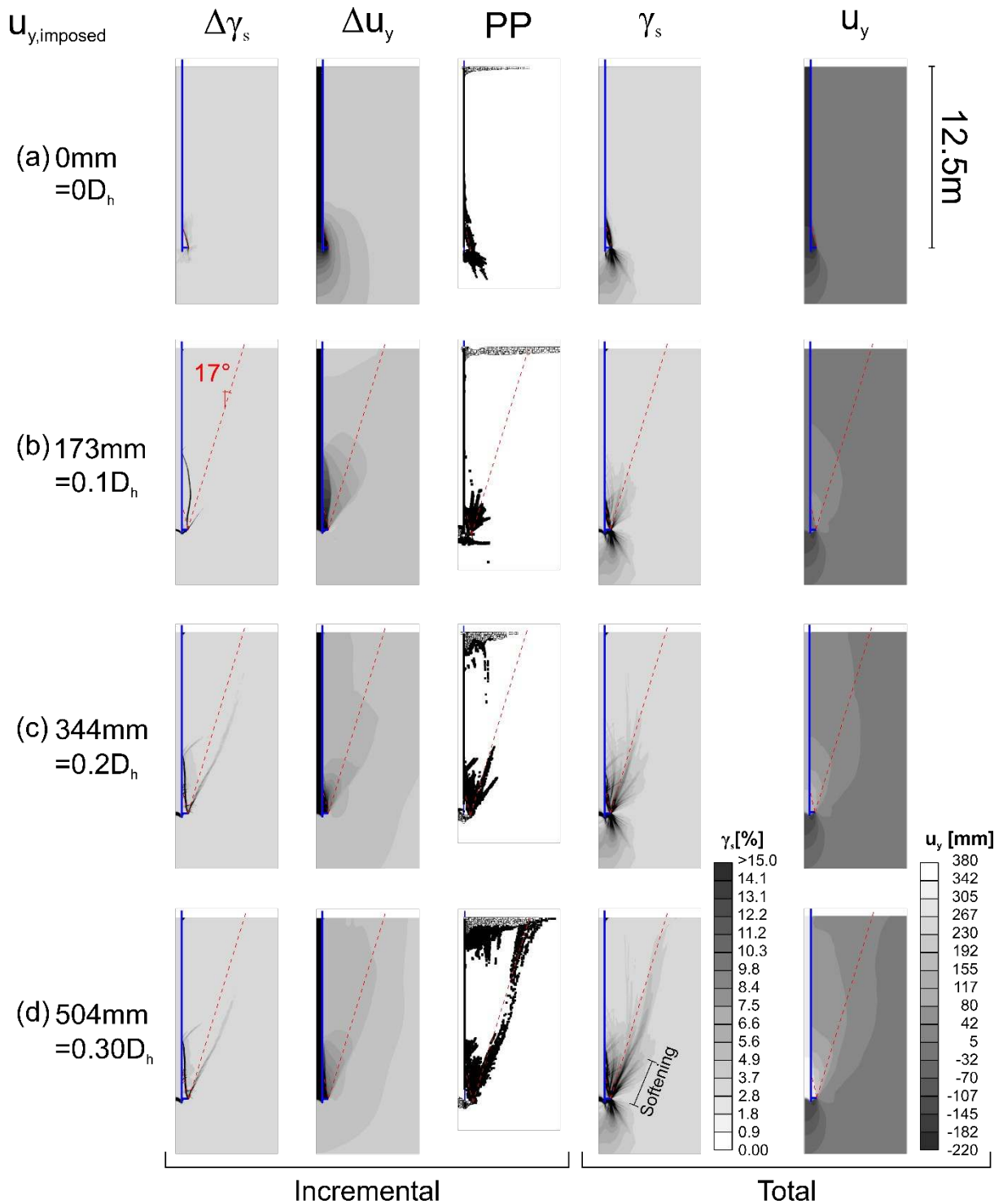
999 Figure 4 Comparison of wished in place centrifuge tests in dense sand from Hao et al. (2018) and
 1000 numerical simulations (Stage 2 - capacity). The two sets of parameters used to calculate the
 1001 analytical criterion of Giampa et al. (2017) correspond to the maximum and minimum density values.

1002



1003
 1004 Figure 5 Comparison of centrifuge test results and finite element simulations (stages 1 & 2). (a)
 1005 U1VD-A, $H/D_h = 5.9$; (b) U1MD, $H/D_h = 4.5$; (c) U1VD-B, $H/D_h = 7.4$; (d) U2VD, $H/D_{h,1} = 7.4$ & $H/D_{h,2} = 5.4$

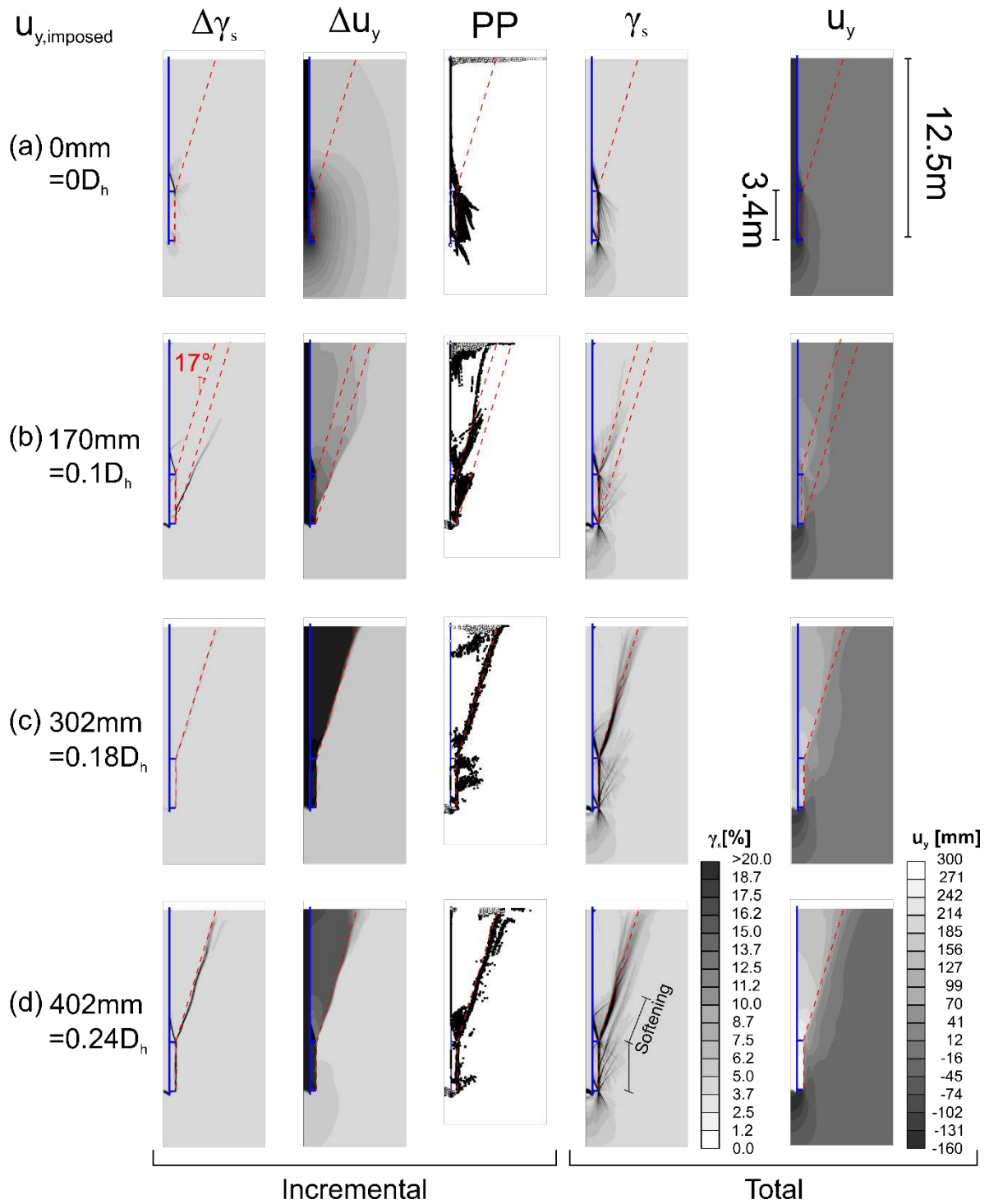
1006



1007
1008
1009
1010

Figure 6 Failure mechanism development at different anchor imposed displacements ($u_{y,imposed}$), single helix in very dense sand (U1VD-B, $H/D_h = 7.4$), the dashed line indicates the failure mechanism assumed by Giampa et al. (2017).

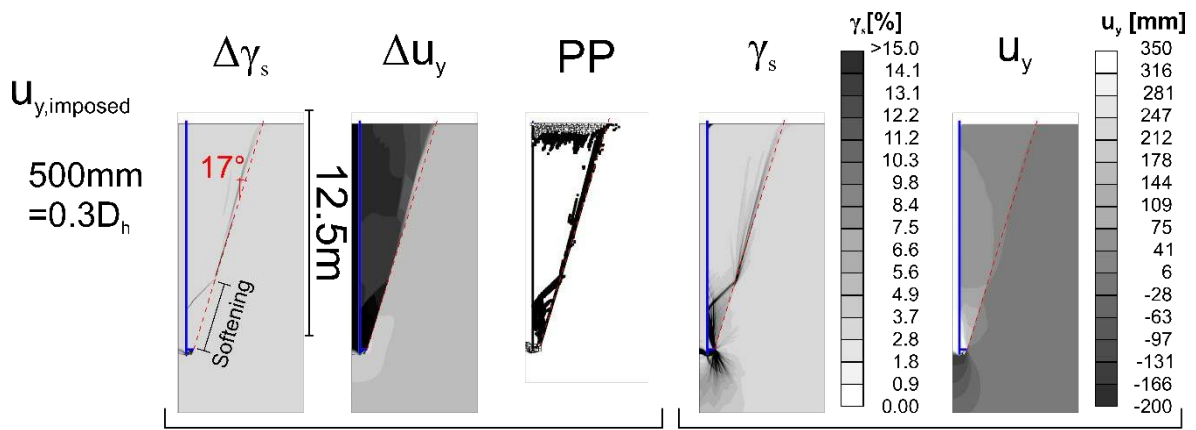
1011
1012
1013



1014
 1015 Figure 7 Failure mechanism development at different anchor imposed displacements ($u_{y,imposed}$),
 1016 double helix in very dense sand (U2VD, $H/D_h=7.4$ & 5.4), the inclined dashed line indicates the failure
 1017 mechanism assumed by Giampa et al. (2017).

1018

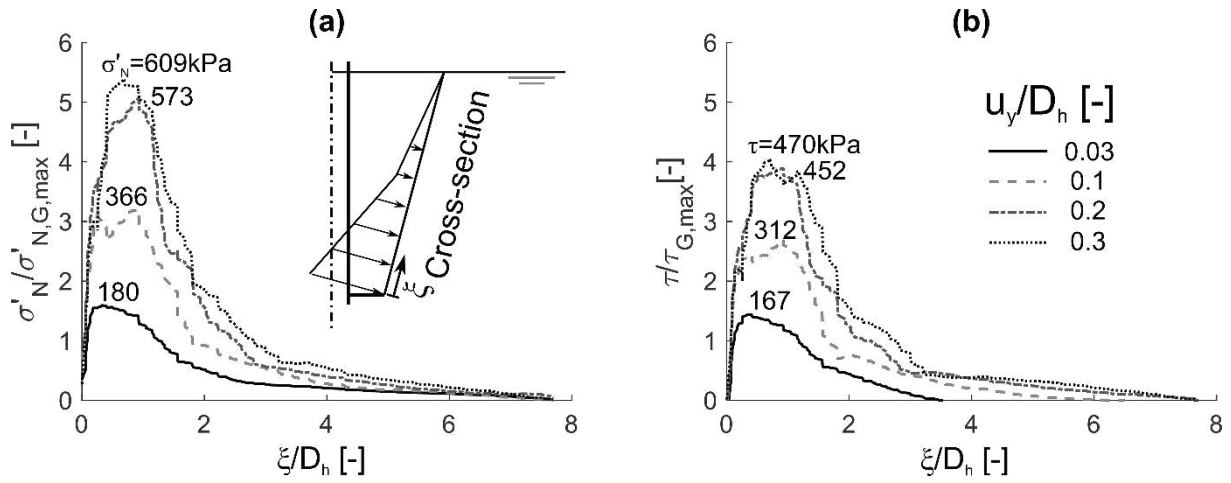
1019



1020
 1021 Figure 8 Comparison of the indicators of failure at the anchor's head ($u_{y,imposed}$), (U1VD-B) and soil-soil
 1022 interface, the dashed line indicates the soil-soil interface

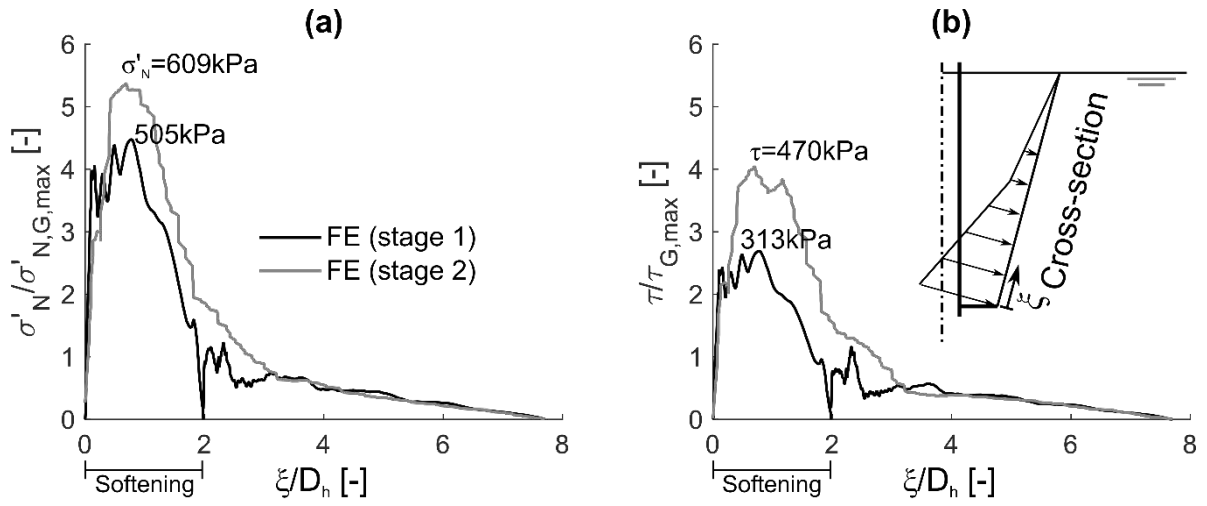
1023

1024



1025
 1026 Figure 9 Consideration of cross-section along the assumed failure mechanism for the single helix
 1027 embedded in very dense sand (U1VD-B), ξ is the distance from the edge of the plate in the direction
 1028 of the cross-section, τ_{max} is the maximum shear stress that could be mobilised ($=\sigma'_N \tan \phi'_{pk}$).

1029

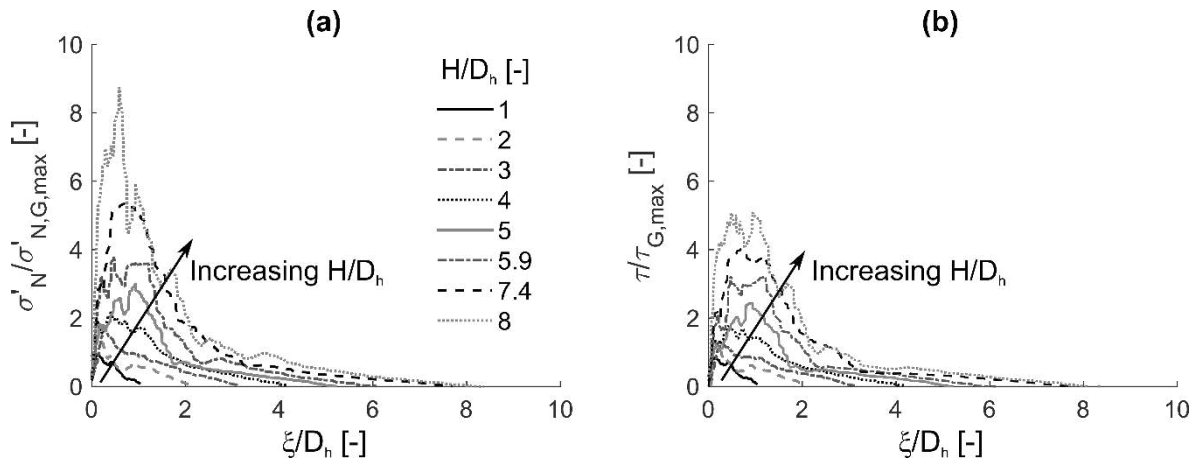


1030

1031 Figure 10 Comparison of the stress distribution along a cross-section (inclined at ψ degrees to the
 1032 vertical) and along the interface elements for the single helix (U1VD-B), after a vertical displacement
 1033 $u_y = 0.3D_h$

1034

1035

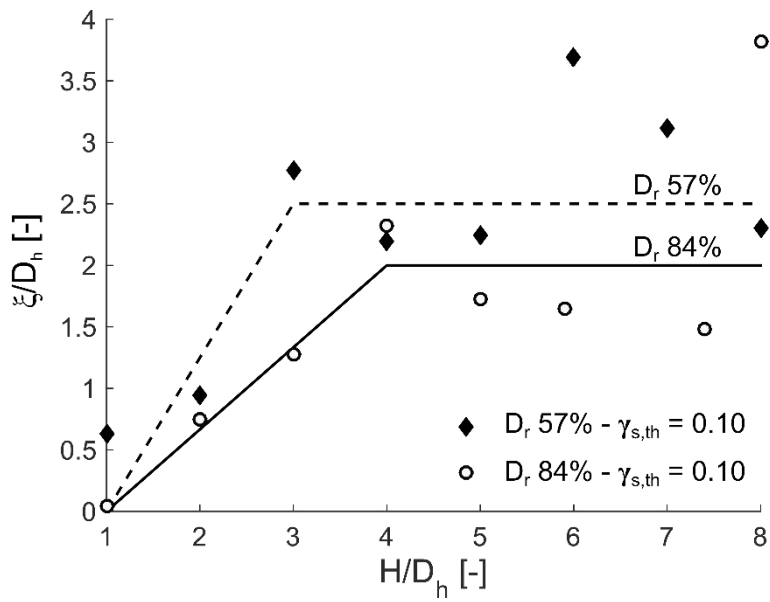


1036

1037 Figure 11 Consideration of the cross-section along the assumed mechanism ($\psi = 17^\circ$) for a single
1038 helix screw anchor ($D_h = 1.7\text{m}$) embedded at different depths in very dense (VD) sand, stage 1
1039 simulations, ξ is the distance from the edge of the plate in the direction of the cross-section, τ_{max} is
1040 the maximum shear stress that could be mobilised ($=\sigma'_N \tan \phi'_{pk}$).

1041

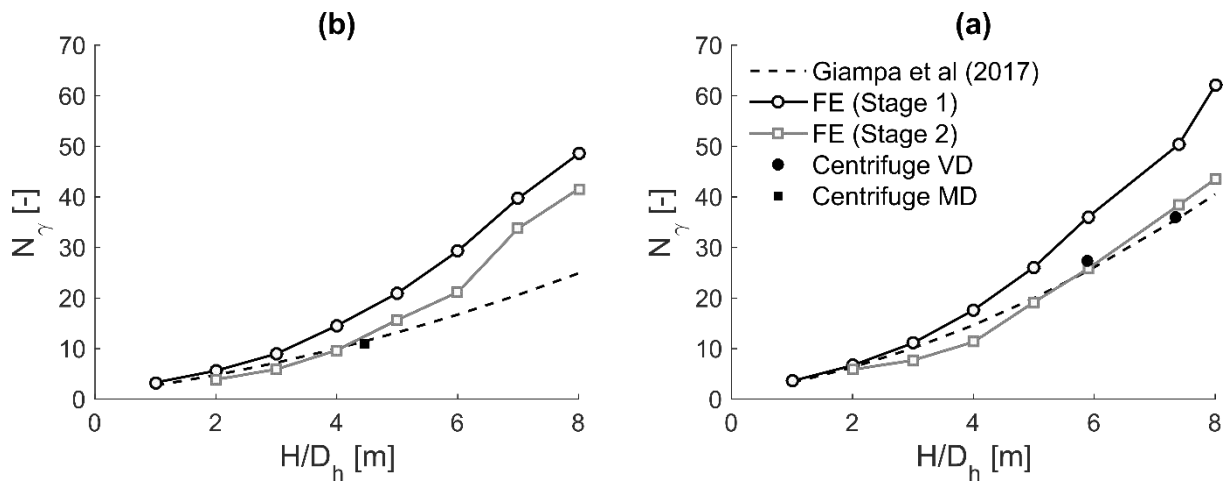
1042



1043

1044 Figure 12 Normalised distance along the failure plane over which the shear strain γ_s is larger or equal
1045 to 10% with respect to normalised plate depth

1046



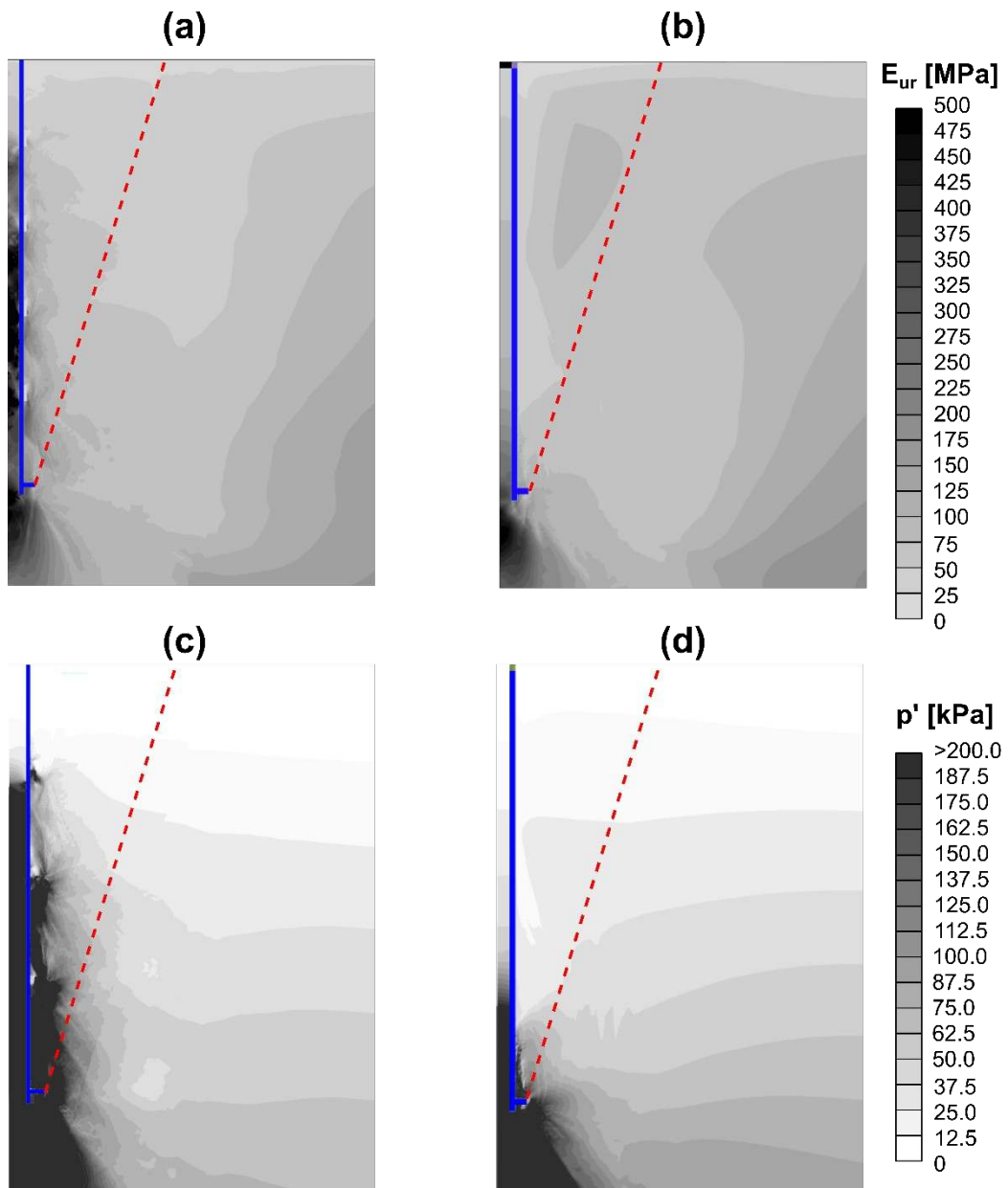
1047

1048 Figure 13 Comparison of bearing factors N_γ for a single helix screw anchor ($D_h = 1.7\text{m}$) at two
 1049 different densities and stage 2 (enhanced capacity). (a) $D_r = 57\%$; (b) $D_r = 84\%$.

1050

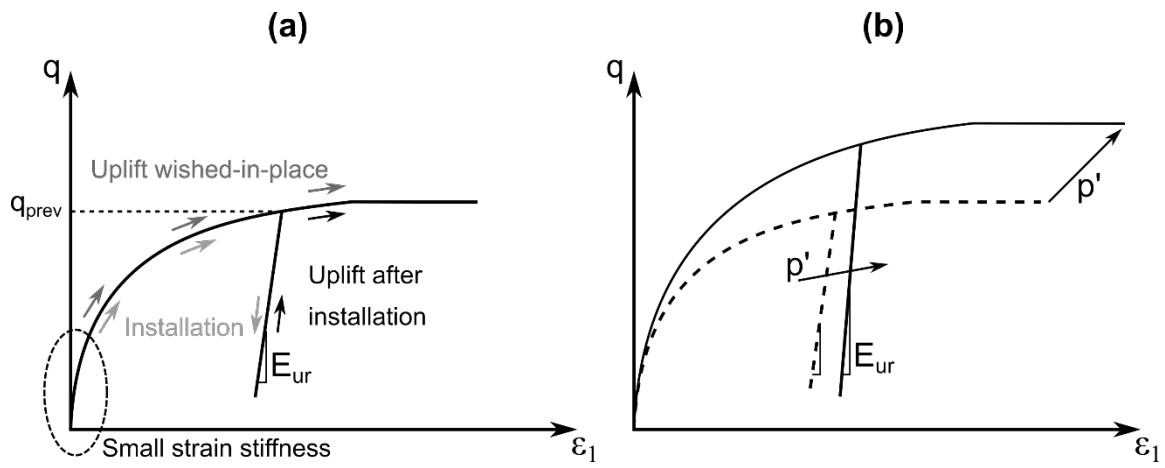
1051

1052



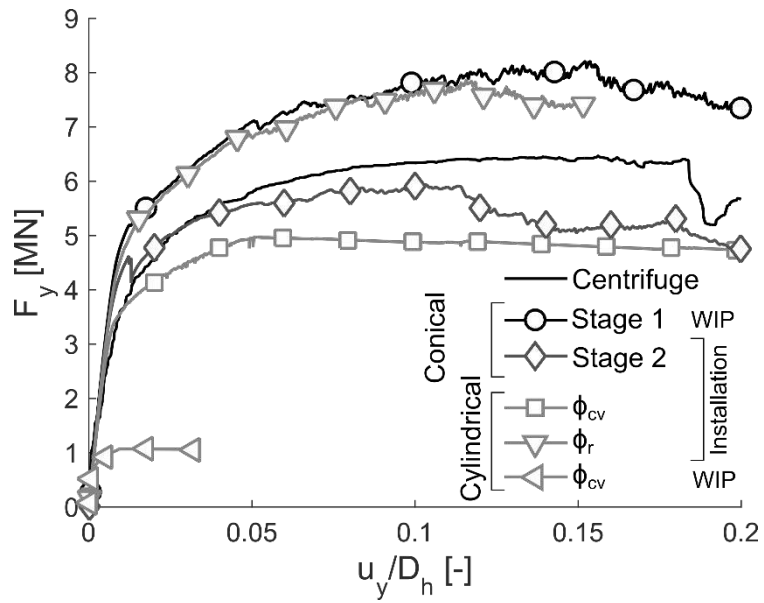
1053
 1054 Figure 14 Comparison of unloading/reloading Young modulus E_{ur} (a-b) and effective average stress p'
 1055 (c-d) after a step-installation procedure (a, c) or after a single compression load (b, d). The inclined
 1056 dashed line indicates the soil-soil interface position in stage 2.

1057



1058
 1059 Figure 15 Idealisation of the installation effect on the soil behaviour, based on the small-strain
 1060 Hardening soil model. (a) Effect of previous shearing; (b) Effect of average stress increase.

1061



1062
 1063 Figure 16 Comparison of centrifuge (U1VD-A, $H/D_h = 5.9$) and numerical solutions with different
 1064 imposed failure mechanisms. Simulations include the installation process (Installation) or are wished-
 1065 in-place (WIP)

1066